Fission product distribution in irradiated safety-tested and as-irradiated AGR-2 TRISO particles

Wright, Karen E.; Stempien, John; Jiang, Wen; van Rooyen, Isabella J.

DOI
10.1016/j.jnucmat.2021.153468

Publication date
2022

Document Version
Final published version

Published in
Journal of Nuclear Materials

Journal of Nuclear Materials 559 (2022) 153468

Contents lists available at ScienceDirect

Journal of Nuclear Materials

journal homepage: www.elsevier.com/locate/jnucmat

Fission product distribution in irradiated safety-tested and as-irradiated AGR-2 TRISO particles

Karen E. Wright[a,b,*], John Stempien[a], Wen Jiang[a], Isabella J. van Rooyen[a]

[a] Idaho National Laboratory, P.O. Box 1625 MS 6000, Idaho Falls, ID 83415, United States
[b] Faculty of Applied Sciences, Department of Radiation Science and Technology, Delft University of Technology, Delft, the Netherlands

ARTICLE INFO

Article history:
Received 13 July 2021
Revised 5 December 2021
Accepted 6 December 2021
Available online 8 December 2021

Keywords:
TRISO
AGR-2
EPMA
Fission product Distribution
BISON

ABSTRACT

Two tristructural isotropic (TRISO)-coated nuclear fuel particles were examined by electron probe microanalysis (EPMA) as part of the Advanced Gas Reactor program. The compacts' average irradiation temperatures ranged from approximately 1260 to 1290 °C. One particle was examined in the as-irradiated condition, while the other was subject to 1600 °C post-irradiation safety testing. This study was undertaken to test a newly-developed EPMA technique to determine fission product masses in TRISO particles on a layer-by-layer basis, and to compare fission product distributions between an as-irradiated and safety-tested particle. Fission product concentration profiles were collected along two radii in each particle, with measured concentrations used to compute the fission product mass in each TRISO particle layer. These measured masses were then compared to those predicted from ORIGEN modeling calculations. Data collected from these measurements show that for these two particles, masses determined via EPMA were within ± 20% of the calculated masses for the rare-earth elements, Mo, Zr, Cs, I, and Pd. Elements that tend to be less homogeneously distributed include Sr, Te, Eu, Ag, and possibly Ba. Measured Ag masses differed by more than 40% from the calculated mass. Lanthanides other than Eu remain primarily within the fuel kernel in the as-irradiated particle but in the safety-tested particle these element masses were divided approximately equally between the kernel and kernel periphery. In both particles, the majority of Sr and Eu accumulated in the carbon-rich kernel periphery, although in the safety-tested particle, Sr and Eu accumulated farther from the fuel kernel than occurred with irradiation alone. A greater mass fraction of mobile elements, such as Cs and I accumulated in the buffer and IPyC in the safety-tested particle as compared to the as-irradiated particle. When fully developed and tested, this mass balance approach to TRISO particle analysis has the potential to provide insight into fuel behavior.

1. Introduction

The AGR-2 experiment was the second fuel irradiation experiment for the Advanced Gas Reactor (AGR) Fuel Development and Qualification program. The purpose of the AGR-2 experiment was to build on the preceding AGR-1 experiment. In contrast to the AGR-1 experiment, which used laboratory-scale fuel fabrication equipment and methods, the AGR-2 experiment used prototype engineering-scale equipment and methods for fuel fabrication.

The AGR-2 tristructural isotropic (TRISO)-coated fuel particle consists of a UCO fuel kernel 425 µm in diameter surrounded by concentric coatings (see Fig. 1a). The UCO kernel is a heterogenous mixture of UO_2 and UC_2 (with small amounts of UC). The coatings include a 100 µm-thick porous carbon buffer, followed by a 40 µm-thick dense inner pyrolytic carbon layer (IPyC) and a 35 µm-thick SiC layer. Finally, a 40 µm-thick dense outer pyrolytic carbon layer (OPyC) overlies the SiC layer [1–8]. The fuel specification for the as-fabricated fuel kernel requires a C/U atomic ratio of 0.40 ± 0.10, an O/U atomic ratio of 1.50 ± 0.20, and a [C + O]/U atomic ratio of ≤ 2.0 [1–8]. Note that Barnes [1] contains the AGR-2 fuel specifications and targeted properties while Refs. [2–7] are original sources for measured fuel properties. Collin's summary of fuel specifications and measured properties [8], was reported in this work.

The outer portion of the kernel differs from the interior of the kernel in that following irradiation, the kernel periphery (KP) is characterized compositionally by the rapid increase in C concentration and the concomitant rapid decrease in U concentration. This compositional change begins at the kernel-KP boundary and continues throughout the entire KP thickness, which varies among the studied particles and is not necessarily uniform around the kernel perimeter. In unirradiated particles, the KP region is composed mostly of uranium oxide; in some particles there is a "skin" at the

* Corresponding author at: Idaho National Laboratory, P.O. Box 1625 MS 6000, Idaho Falls, ID 83415, United States.
E-mail address: Karen.Wright@inl.gov (K.E. Wright).

https://doi.org/10.1016/j.jnucmat.2021.153468
0022-3115/

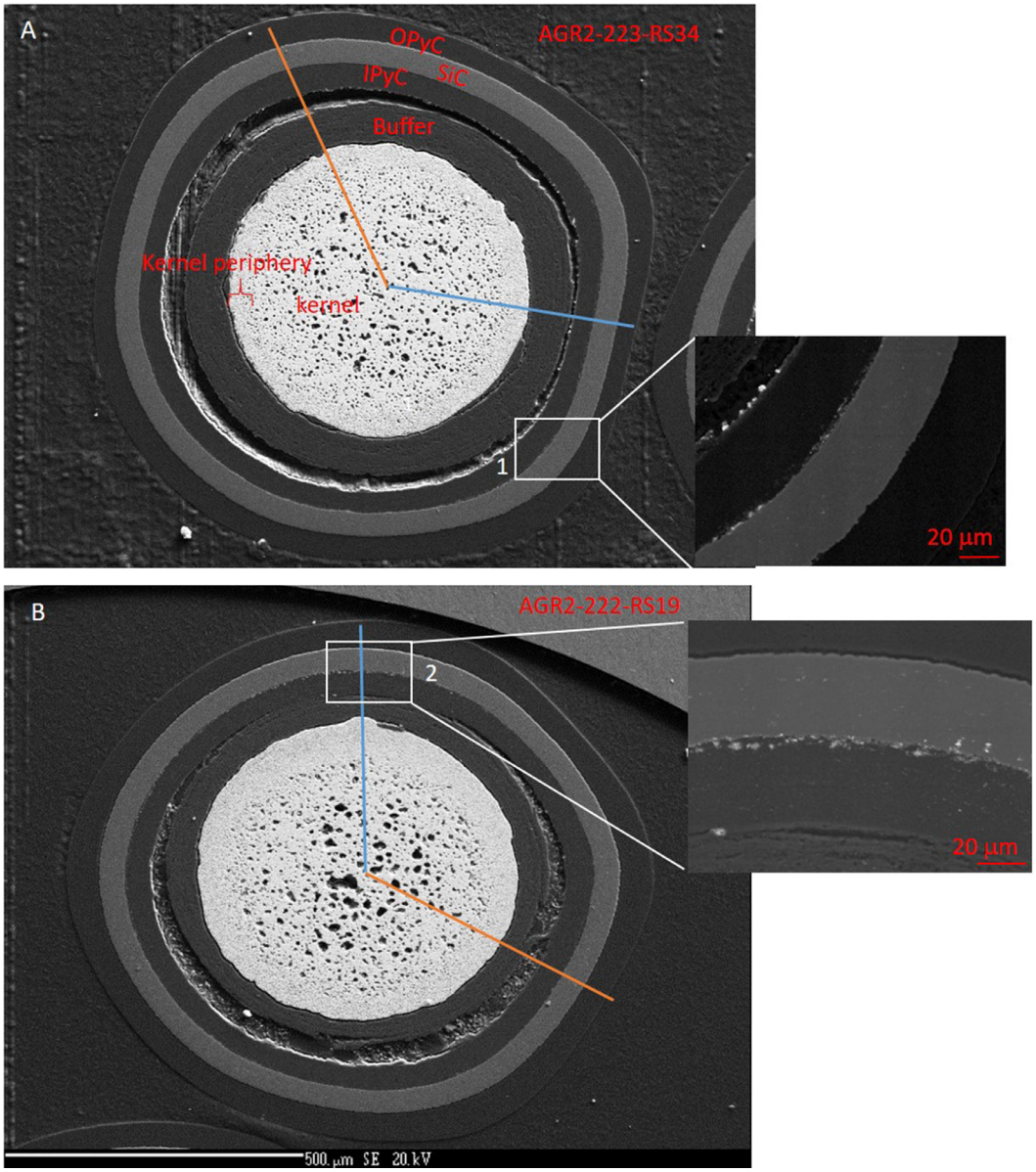

Fig. 1. (a, b). Electron microscope images of the two examined particles showing the path of quantitative radial chemistry measurements (orange and blue lines). (A) Secondary electron image of as-irradiated Particle AGR2-223-RS34, and (B) Secondary electron image of safety-tested Particle AGR2-222-RS19. The TRISO layers are labeled in image A. Both images were obtained using the same magnification. Note the gap between the buffer and IPyC layers in each particle. Boxes 1 and 2 (backscattered electron images) show the locations of high-Z precipitates along the IPyC-SiC boundary. (For interpretation of the references to colour in this figure legend, the reader is referred to the web version of this article.)

kernel-buffer interface that is primarily uranium carbide [9]. In additional to different stoichiometry in the KP than in the bulk of the kernel, after irradiation, the KP often has much smaller pores than those located toward the center of the kernel.

Fission product (FP) distribution in irradiated nuclear fuels has been studied by electron probe microanalysis (EPMA) for several decades. The use of EPMA is advantageous for several reasons. First, the energy resolution of EPMA is typically on the order of 10 eV, compared to ~125 eV for the modern silicon drift detectors used in scanning electron microscopes [10]. Second, the EPMAs used for irradiated specimens are equipped with W-alloy shielding to: (1) reduce detector background noise; (2) reduce the signal to background noise ratio changes that occur when sample-to-detector distance is altered during stage movement; and, (3) preserve detector life. Finally, the high currents (200–300 nA) employed by EPMA during irradiated specimen analysis can improve detection limits by a factor of 10 or more [11].

Previous EPMA efforts examined FP distribution [12–14], precipitate composition [14], and Cs chemical speciation in the buffer [15,16] of layered fuel particles, with one study reporting on FP distribution in AGR-1 fuel particles [17]. This study expands on these efforts by estimating the FP product mass in each particle layer, and compares these distributions between two similarly irradiated particles, one of which was safety-tested after irradiation.

1.1. Objectives

This study has several objectives. Firstly, the mass-balance-by-EPMA method will be described, with results of the executed method presented for an as-irradiated TRISO particle and an irradiated-and safety-tested particle. Examples of fission product behaviors illustrated by the two particles will be compared, with findings from this study compared to findings from other fission product studies. Secondly, in order to test the model accuracy, fis-

sion product masses determined by EPMA will be compared to those predicted by ORIGEN modeling. Thirdly, possible explanations for observed particle behavior will be presented. Finally, this study will demonstrate the utility of using EPMA for such quantitative studies.

2. Experiments

2.1. Irradiation and safety testing

Compacts 2-2-2 and 2-2-3 are two of a total of 48 AGR-2 UCO fuel compacts, each containing approximately 3176 particles, which were irradiated in the Advanced Test Reactor (ATR) at Idaho National Laboratory (INL) as described by Collin [18]. These compacts were subjected to post-irradiation examination (PIE) at Oak Ridge National Laboratory (ORNL). Following irradiation, a subset of compacts including Compact 2-2-2 was safety tested using the Oak Ridge National Laboratory (ORNL) Core Conduction Cooldown Test Facility to evaluate the release of FPs upon heating. Morris et al. [19] discuss the procedures and equipment for this process.

In order to measure fission products outside of the particles' SiC layers and to prepare individual particles for examination, it was necessary to separate the particles from the compact using a process known as deconsolidation-leach-burn-leach (DLBL), which is an electrolytic deconsolidation process used to separate the particles from the compact matrix. Details of the deconsolidation process can be found in [20]. A subset of particles was separated from the rest of the particles prior to the "burn" step of DLBL; therefore, this subset still had intact OPyC layers.

Both particle subsets from Compacts 2-2-3 and 2-2-2 were subjected to gamma counting using a process referred to as "irradiated microsphere gamma analysis" (IMGA) [21] to determine the fraction of retained high yield isotopes, known as the measured-to-calculated (M/C) ratio. It is the ^{110m}Ag M/C value that is the primary criteria for particle selection for scanning electron microscopy (SEM) analysis [22]. Efforts were made to select particles with very high ^{110m}Ag M/C and particles in which there was very low, or non-detectable quantities of ^{110m}Ag. In this way it was possible to study particles with varying temperature histories, as ^{110m}Ag retention is thought to be influenced strongly by temperature [23].

Following PIE, sample preparation, and various analyses at ORNL, a subset of prepared particles was sent to INL for further examination. Six AGR-2 particles were selected for EPMA analyses at INL. For this study, irradiated particle AGR2-223-RS34 and irradiated and safety-tested particle AGR2-222-RS19 were selected as test cases for the EPMA mass-balance method.

The temperature, burnup, and fluence are average values for the entire compact from which the particles were selected and are shown in Table 1. While the two particles selected for this work have similar irradiation histories and their respective compacts appear to have experienced similar temperatures, particle AGR2–223-RS34 retained 84% of its ^{110m} Ag while particle AGR2-222-RS19 (measured after the safety test) retained 20% of its ^{110m} Ag. According to Hawkes [24], the average minimum temperature (TA Min) for Compact 2-2-3 is 1161 °C while the average maximum temperature (TA Max) for Compact 2-2-2 is 1354 °C, which means that the maximum temperature difference between particle AGR2-222-RS19 and AGR2-223-RS34 is 193 °C. Alternatively, if particle AGR2-222-RS19 experienced the compact's TA Min of 1189 °C, the two particles could be the same temperature. However, because Ag retention is thought to be a function of the particle's temperature history [23], the high retained Ag in particle AGR2-223-RS34 suggests that this particle experienced a lower time-average, volume-average (TAVA) temperature than particle AGR2-222-RS19 [22].

Table 1
The irradiation and safety-testing parameters for the two examined AGR-2 particles [1–8,24,26–27].

Parameter	AGR2–223-RS34	AGR2–222-RS19
^{235}U enrichment	14.03	14.03
% FIMA average burnup	10.82	12.57
Time-average, volume average temperature, °C	1261	1287
Approximate fast fluence [E> 0.18 MeV] (x 10^{25}), n/m^2	2.99	3.39
Measured to calculated ^{110m} Ag ratio	0.84	0.2*
1600 °C safety test (hours)	Not applicable	300

*measured after safety test.

However, despite the possible temperature differences, AGR2-223-RS34 appears to exhibit non-volatile fission product behavior similar to other as-irradiated particles with similar burnup. While that particular particle retained an anomalously high amount of silver, when compared to particle AGR2-223-RS06 (from the same compact), which lost most of its silver, the less-volatile fission products such as Ru behave much more similarly to the as-irradiated compact 2-2-3 compared to the irradiated and safety-tested particles of safety-tested compact 2-2-2 [25]. Similarly, van Rooyen et al. [25] demonstrated that safety-tested particles from AGR-1 and AGR-2 exhibit specific fission product behaviors that appear distinct from that of non-safety tested particles. Despite the work of van Rooyen et al. [25], it is important to recognize that one of the limitations of irradiated materials analysis, including this study, is that due to the large number of particles per compact and the substantial per-particle analysis cost, relatively few particles have been analyzed relative to the number of available irradiated particles; therefore, it is difficult to ascertain whether results from one or a few particles are representative of the remaining particles in the compact, especially when intra-compact variability is known to exist. None-the-less, van Rooyen et al. [25] show that among the few particles analyzed by EPMA, as-irradiated particles appear to exhibit different fission product distributions when compared with irradiated and safety-tested particles.

2.2. Sample preparation

Fig. 1 shows the two particles examined in this work. Particle AGR2-223-RS34 was analyzed in the as-irradiated state, while particle AGR2-222-RS19 was irradiated and subsequently safety tested at 1600 °C for 300 h. The orange and blue lines show the radial paths analyzed for quantitative chemical composition. The locations of the analyzed paths were chosen based on the anticipation that the elemental concentration profiles measured would have significant differences due to buffer-IPyC gaps created by buffer delamination or minor kernel irregularities along the KP outer perimeter. Boxes 1 and 2 show the location of precipitates occurring along the respective particles' IPyC-SiC boundaries.

Sample preparation occurred at ORNL following methods described by Hunn et al. [20]. Briefly, particles were mounted in epoxy using vacuum back-potting to improve particle integrity. Cured mounts were then ground and polished to mid-plane using a Buehler Minimet 1000. Prior to EPMA analysis polished mounts were coated with 15 nm of aluminum to ensure sample conductivity.

2.3. Electron probe microanalysis

Electron probe microanalysis was performed at Idaho National Laboratory's Irradiated Materials Characterization Laboratory using a Cameca SX100R electron probe microanalyzer, which is specifically designed for the analysis of highly radioactive specimens. To

that end, the instrument's electronics and detectors are shielded to 3 Ci of ^{137}Cs. Specific EPMA methodology is detailed in Appendix A.

Quantitative radial traverse data were collected along the traverse paths shown in Fig. 1 using Probe for EPMA software v. 12.4.6 (©Probe Software). For each particle, one radius was measured in a region in which there was a gap between the buffer and IPyC, and a second radius was measured in a region that lacked a gap, or the gap was small. The radial traverse locations were selected to compare particle regions that would likely exhibit the greatest compositional differences, based on observations from previous examinations [17]. The distance between analyzed points varied from 2 to 5 μm depending on the region of the particle being measured. Regions where the chemistry changes were more rapid (e.g. KP, IPyC-SiC interface) used a 3 μm and 2 μm inter-point interval, respectively. In all other regions the inter-point interval was 5 μm. All X-ray collection programs used the Pouchou and Pichoir (PAP) matrix correction algorithm and mass absorption coefficients for $Z < 92$ [28] with some exceptions. U mass absorption coefficients (MACs) used were those of Farthing and Walker [29], while the O kα in U MAC came from Poeml and Llovet [30].

2.4. Calculation method

The approach to evaluating quantitative FP distribution differences between safety-tested and as-irradiated particles was to take the fission product measurements derived from the radial traverses in each of the two particles and use those data to estimate the mass of each elemental fission product present in each of the various particle layers.

Quantitative weight percent EPMA data from the radial traverse measurements in each particle were converted to an elemental mass in each particle, subdivided according to the particle layer (e.g., kernel, buffer, IPyC, etc.). The procedure and assumptions employed were as follows:

1. The weight percent of the measured element at a specific location along the measured radial traverse is assumed to be homogeneous for a hemispheric shell (Fig. 2) of the TRISO particle with a thickness equivalent to the traverse step-size. At all times the beam interaction volume is smaller than or equal to the step size so that the beam interaction volume does not need to be considered. Each examined particle hemisphere is divided into approximately 100 concentric hemispheric shells.
2. The volume of the hemisphere shell of the measured traverse step-size width is calculated.
3. As it was not measured specifically, the buffer density is assumed to conform to those values provided in the fuel fabrication specifications [1,8,31]. The buffer layer densifies during irradiation; based on observations of the particles in Fig. 1(a, b), it doubles for AGR2-223-RS34 and increases by a factor of 2.85 for AGR2-222-RS19. These values are calculated by measuring the buffer thickness along the two radial traverses for each sample, averaging them, and then comparing the result to the fabrication specification of a 100 μm-thick buffer. This assumes that the particle is spherical and that the cross section is taken at exactly midplane. However, it is difficult to judge how close the cross section is to midplane, and the particles are not perfectly spherical. Detailed serial cross sectioning, layer dimensional measurements, and fits of these measurements to a sphere would be needed to improve the accuracy of the buffer volume changes [32].
4. The mass of each of the hemispheric shells in each TRISO layer is computed from the estimated volume and density.
5. The weight fraction is multiplied by the mass of the hemisphere shell to arrive at a mass in grams of the element, in each hemispheric shell.
6. The procedure is repeated for each hemispheric shell for the first measured radial traverse.
7. The procedure is then repeated for the other radial traverse to account for spatial variation in layer morphology and fission product content.
8. The total mass of the element in the particle is calculated by adding all the shells from both hemispheres together. Similarly, the process also allows for determining mass in half the particle, or by TRISO particle layer.

This procedure required the assumption that the fission product distribution was symmetrical. Some over- or under-estimation may occur with this method because the fission product distribution may not be symmetrical and each EPMA traverse only accounts for a small volume of one hemisphere of the original particle. In addition, radial traverse measurements were obtained where the most variation was expected and thus were not necessarily180 ° from one another.

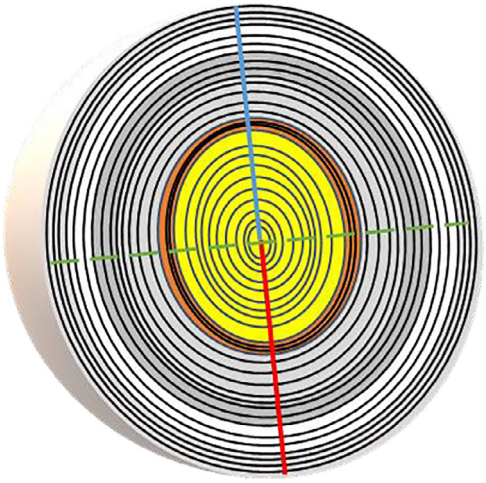

Fig. 2. Schematic of a TRISO hemisphere with concentric circles showing hemispheric shells (separated by the green dotted line) in the various TRISO layers. Red and blue lines represent hypothetical EPMA traverse paths. In the actual TRISO particles, the shells are no more than 5 μm thick. (For interpretation of the references to colour in this figure legend, the reader is referred to the web version of this article.)

3. Results

3.1. Morphology

Both studied particles are characterized by a nearly complete delamination of the buffer from the IPyC at the specific plane of polish. However, it is possible that the buffer-IPyC interface has a different morphology (e.g., complete delamination or no delamination) at another plane within the particle. In addition, the KP region in both particles exhibits variable thickness, ranging from approximately 13–60 μm thick, as measured along the radial traverses. Finally, the KP is quite distinct from the kernel central region in that the KP is characterized by a large number of small-diameter pores ($\sim <$ 1 μm in diameter), in contrast with the center of the kernel, which is typified by fewer, much larger pores (~1–50 μm in diameter).

3.2. Fission product distribution

3.2.1. Cs, Xe, I

Cs, Xe and I are volatile fission products, whose behavior in the TRISO particle is of particular interest due to the possibility of re-

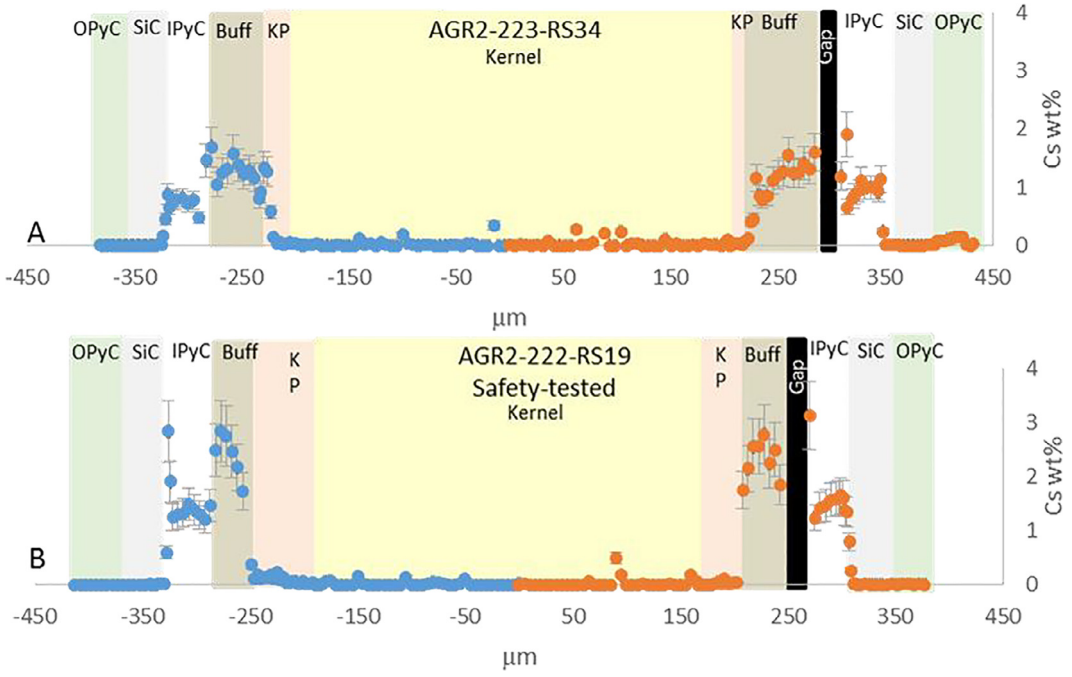

Fig. 3. (a, b). Quantitative radial traverses of Cs for both examined particles. The non-gap side of the particle is shown in blue while the gap side is shown in orange. 99% confidence interval error bars are shown. Where they are not visible, the error bars are smaller than the symbol. (For interpretation of the references to colour in this figure legend, the reader is referred to the web version of this article.)

lease from the particle. Fig. 3(a, b) is the first of numerous figures presented in this work that illustrate EPMA analytical measurements with 99% confidence interval error bars. A confidence interval is a statistical designation that provides a range of possible values for a measurement. For a 99% confidence interval, that means that if a particular measurement were performed 100 times, the true value of the measurement would be present within the range of 99 of those values. The error bars in the plots illustrate that range.

Fig. 3(a, b) shows the Cs concentration profiles for both particles. For both particles, the profile on the gap side and the non-gap side are similar to one another. In addition, for both particles, the Cs concentration is slightly higher in the kernel perimeter than in the kernel center. Regardless of whether or not there is a gap, both particles show elevated concentrations in the buffer and IPyC as compared to the kernel. Cs concentrations in the buffer generally exceed those in the IPyC. Possibly the greater porosity and attendant surface area afforded to the buffer allows for greater Cs sorption relative to the IPyC, and Cs concentration decreases in the IPyC accordingly.

There are differences in Cs concentration profiles between the safety-tested (AGR2-222-RS19) and the as-irradiated particle (AGR2-223-RS34). The peak Cs concentration in the buffer of the safety-tested particle is on the order of 50–100% greater than in the as-irradiated particle. In addition, on the non-gap side of the safety-tested particle, the Cs concentration is elevated at the IPyC-SiC interface.

While Cs concentration profiles are symmetrical in both studied particles (Fig. 3a, b), I and Xe profiles are somewhat more complex. In the as-irradiated particle, I and Xe concentrations on the non-gap side peak at the KP-buffer boundary and are roughly double the highest concentrations on the gap side of the particles. The bulk of the iodine is located in the KP and buffer of the as-irradiated particle while I in the safety-tested particle is primarily located outward, in the buffer and IPyC. Iodine is largely absent in the kernels of both particles, with only a few points with detectable iodine noted during analysis.

In the as-irradiated particle, Xe concentration peaks at the KP-buffer boundary, with the bulk of Xe located in the KP and buffer; whereas in the safety-tested particle, Xe is symmetrically distributed, with the bulk located in the buffer and IPyC. Xe is largely undetected in the kernel of the safety-tested particle.

3.2.2. Sr, Ba, Te, Eu

Fig. 4(a-b) shows the Sr concentration profile for both studied particles. In contrast to Cs, Xe, and I, the Sr concentration profile is less symmetrical across both particles. Specifically, the Sr peak concentration is approximately 1.7 times greater in the KP on the non-gap side of particle AGR2-223-RS34 as compared to the gap side of that particle. For safety-tested particle AGR2-222-RS19, the peak KP concentration difference is a factor of five when the non-gap side is compared to the side with a gap. For both particles, the Sr concentration increases in the KP and reaches its maximum on the KP side of the KP-buffer boundary. Concentrations then decline suddenly at the KP-buffer interface.

Interestingly, for both particles, concentration gradients appear relatively constant in the buffer, IPyC, SiC, and OPyC, but overall, the concentration appears to decrease in a stepwise manner toward the particle periphery. Between the IPyC and SiC on the gap side of the as-irradiated particle and between the IPyC and SiC on the non-gap side of the safety-tested particle, flat concentration profiles are interrupted by a concentration spike at the interface between two layers. In some instances, these flat concentration profiles are punctuated by local minima at an interface. For example, in the as-irradiated particle, a minimum occurs at the SiC-IPyC interface on the non-gap side. A similar minimum occurs in the safety-tested particle on the gap side. While the phenomena causing the minima are not understood, the minima may result from porosity changes between adjacent layers that could be inherent to the materials or could possibly be produced by polishing adjacent materials with dissimilar hardness. Alternatively, they may result from an EPMA measurement artifact. The 20 keV beam interaction volume can be calculated by the Monte Carlo modeling program, Casino v.2.51 [33]. In the IPyC, the beam interaction volume is ap-

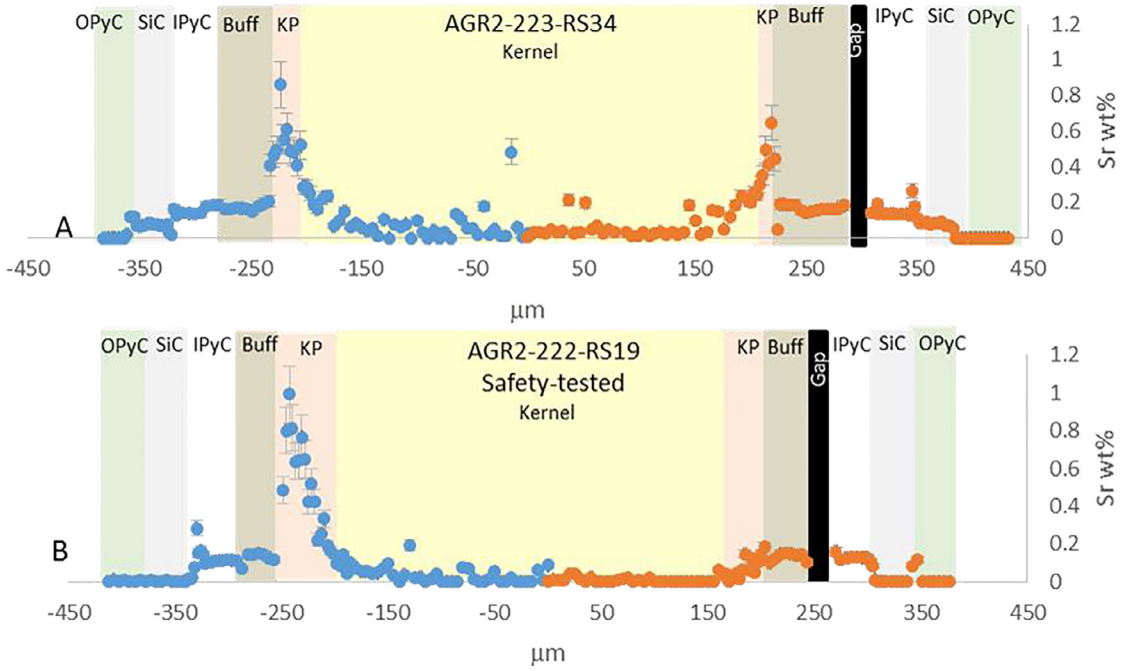

Fig. 4. (a, b). Shows the quantitative radial traverses of Sr for both examined particles. The non-gap side of the particle is shown in blue while the gap side is shown in orange. 99% confidence interval error bars are shown. Where they are not visible, the error bars are smaller than the symbol. (For interpretation of the references to colour in this figure legend, the reader is referred to the web version of this article.)

proximately 3 µm in diameter while in the SiC it is approximately 2 µm. Measurement near a boundary may result in two disparate compositions captured within the same beam interaction volume. Since EPMA (as well as scanning electron microscopy) data reduction assumes a chemically homogeneous beam volume, it is possible that measurement close to the boundary has resulted in secondary fluorescence or other artifacts that decrease analysis accuracy.

Finally, safety testing appears to decrease the average Sr concentration inside the kernel and generally flattens the concentration profile. Strontium concentrations in the as-irradiated particle's SiC layer are notably higher than those observed in the safety-tested particle. Sr is volatile and may be preferentially lost during the safety testing procedure. The Ba, Te, and Eu profiles are similar to Sr (data not shown).

3.2.3. *IPyC-SiC interface*

Fig. 5(a–h) shows the behavior of select fission products near the IPyC-SiC interface for both sides of both particles.

Pd is of interest because in instances where the IPyC has fractured or otherwise been degraded such that a portion of the SiC layer was exposed to the interior of the particle, Pd may interact chemically with the SiC [34], while Ag is of interest because it appears to be released easily during irradiation [35]. Elements such as U, Pd, Zr, Ru, and Mo are of interest as they have been noted to occur in high-Z features along the IPyC-SiC boundary [22] and into the SiC layer. Fission products Ba and Cs have been included as they occur in abundance relative to elements such as Ru, Mo, and Zr. High-Z features tend to form at the IPyC-SiC interface as well as within the SiC layer (Fig. 1), primarily along grain boundaries [36]. Such features are much smaller than the approximately 2 µm diameter EPMA beam volume in the SiC; thus, EPMA traverses in this region cannot distinguish between the high-Z features and the surrounding matrix.

Fig. 5(a, c) shows that for as-irradiated particle AGR2-223-RS34, Pd is detected in the IPyC 10 µm prior to the SiC layer on the non-gap side of the particle and is detected throughout the SiC layer in concentrations up to ten times higher than those observed on the gap side of the particle. U is detected in the IPyC on both sides of the particle, but occurs in higher concentrations on the non-gap side of the particle. U concentrations in the IPyC greatly exceed Pd concentrations in the IPyC on both sides of the particle (Pd is not detected in the IPyC on the gap side until the IPyC-SiC interface); however, within the SiC layer these trends are reversed. Whereas as Pd is detected throughout the SiC on both sides of the particle, U is not detected beyond 4 µm into the SiC on the non-gap side and is not detected in the SiC on the gap side of the particle (Fig. 5(a, c)). Silver is not detected in the IPyC of either side of AGR2–223-RS34 but is detected on the non-gap side of the particle where it penetrates approximately 2 µm into the SiC layer.

Fig. 5(b, d) shows that Cs and Ba behavior is similar on both sides of the particle, with elevated concentrations in the IPyC falling by two orders of magnitude once these elements enter the SiC layer. Cs and Ba occur sporadically throughout the SiC layer on the gap side of the particle, but were not detected beyond 8 µm into the SiC layer on the non-gap side. Zr, Ru, and Mo are detected in the IPyC on both sides of AGR2-223-RS34, with Zr occurring in higher concentrations than Ru and Mo, which are similar in concentration. Zr, Ru, and Mo penetrate the SiC layer on the non-gap side of the particle in roughly equal concentrations. On the gap side of the particle, an isolated occurrence of Ru is located 4 µm into the SiC layer.

Fig. 5(e, g) shows that for irradiated and safety-tested particle AGR2-222-RS19, the maximum Pd concentration occurs in the IPyC on the non-gap side of the particle (Fig. 5e); however, Pd is detected throughout the SiC layer on both sides. On the non-gap side of the particle U and Pd concentrations are similar in the IPyC; however, as the SiC layer boundary is approached, Pd concentrations slightly exceed uranium concentrations on both sides. In the SiC layer of both sides of the particle, Pd concentrations are on the order of 10 times higher than U concentrations. Uranium is detected sporadically in the SiC layer to a depth of 28 µm on the non-gap side, but not beyond 10 µm on the gap side of the particle. Silver is detected at three points: 6, 4, and 2 µm before the

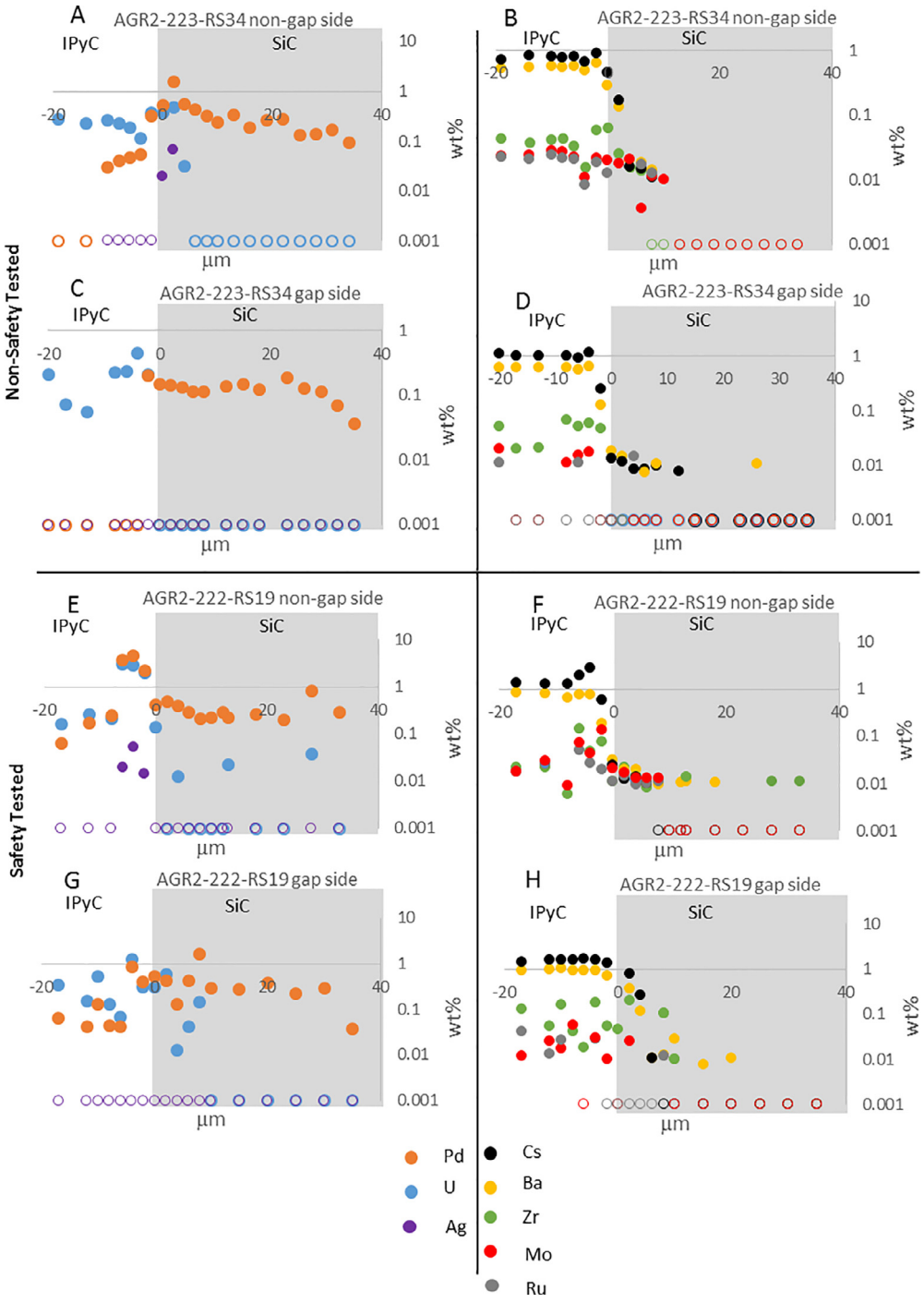

Fig. 5. (a–h). Shows the U, Pd, and Ag concentration profiles across the IPyC-SiC boundary for both a) AGR2-223-RS34 (non-gap side), and c) AGR2-223-RS34 (gap side). Cs, Ba, Zr, Mo and Ru concentration profiles across the IPyC-SiC boundary are shown for both b) AGR2-223-RS34 (non-gap side), and d) AGR2-223-RS34 (gap side). U, Pd, and Ag concentration profiles across the IPyC-SiC boundary are shown for e) AGR2-222-RS19 (non-gap side), and g) AGR2-222-RS19 (gap side). Cs, Ba, Zr, Mo and Ru concentration profiles across the IPyC-SiC boundary are shown for both f) AGR2-222-RS19 (non-gap side), and h) AGR2-222-RS19 (gap side). Points where the measurement was below the detection limit are indicated by open circles. Note that all plots are semi-log plots to better illustrate minor element behavior. 99% confidence interval error bars are smaller than the symbols.

SiC boundary on the non-gap side of AGR2–222-RS19 and may be associated with high-Z features located along the IPyC-SiC interface. No Ag was detected in the SiC layer on the non-gap side of the particle, nor in the IPyC or SiC layers on the gap side of the particle.

Fig. 5(f, h) show that Cs and Ba both show elevated concentrations in the IPyC of both sides of particle AGR2-222-RS19 but that concentrations fall by two orders of magnitude once the SiC layer is encountered. Ba penetrates into the SiC layer approximately 20 µm on both sides of the particle. Zr is present in similar concentrations within the IPyC of both sides of the particle, but while Zr is detected sporadically through the SiC layer on the non-gap side of the particle, it is not detected beyond 10 µm into the SiC layer on the gap side of the particle.

In the IPyC of both sides of the as-irradiated particle, Zr concentrations exceed Mo and Ru concentrations, which are roughly

equal to each other. For the safety-tested particle, Zr concentrations in the IPyC are slightly higher on the gap side of the particle but Mo and Ru are roughly equal. On the non-gap side of the particle, there is no clear pattern for Zr, Ru, and Mo concentrations—they are all roughly similar (Fig. 5(f, h)).

The IPyC-SiC interfacial region is complex. The following summarizes observations for this region for both particles:

- In the IPyC of both sides of both particles, U concentrations generally exceed Pd concentrations, except within 2–6 μm of the SiC boundary. In this region on both sides of the as-irradiated particle, U slightly exceeds Pd concentrations whereas the converse is true for the safety-tested particle.
- In the SiC layer of both sides of both particles, the Pd concentrations are much larger than the U concentrations. U was not detected in many of the measured points in the SiC layer of either particle.
- Ba and Cs behavior is similar for both sides of both particles, where both elements are elevated in the IPyC layer but drop by a factor of 100 as the SiC is encountered.
- Zr concentrations exceed Mo and Ru in the IPyC on both sides of the as-irradiated particle and on the gap side of the safety-tested particle; Zr penetrates into the SiC layer of the non-gap side of both particles and into the SiC layer of the gap side of the safety-tested particle.
- For both particles, a larger number of the measured elements were detected on the non-gap side of the particles compared with the gap side of the particles.

3.3. Carbon and oxygen ratios in the kernel periphery

Carbon and oxygen concentrations were measured during the radial traverse point measurements. Figs. 6 and 7 show O:C ratios and quantitative X-ray maps of Sr, O, C, and U on both sides of both particles. Fig. 6a shows that on the gap side of the as-irradiated particle, the O:C ratio at the KP inner boundary is approximately 0.6 and falls in a linear manner to about 0.01 at the interface between the KP and the buffer. Fig. 6b shows that the O:C ratio on the non-gap side is approximately 1.7 at its inner boundary and falls similarly in a linear fashion to a value of 0.02 at the KP-buffer interface. Fig. 6(c, e, g, i) shows the 13 μm-thick gap-side KP for Sr, O, C, and U, respectively. In this region, Sr content increases while O:C ratios decline. Similarly, Fig. 6 (d, f, h, j) shows the 31 μm-thick non-gap side KP with the thicker Sr accumulation zone evident. Ba, Te, and Eu behave similarly (data not shown). The similarity in Sr and Eu behavior is expected given that they have similar oxide-carbide equilibria and tend to favor the carbide phase at the burnups and kernel stoichiometry of this AGR-2 fuel [37].

Fig. 7(a, b) shows that on both sides of the safety-tested particle, the O:C ratios in the KP layer are more scattered than on the as-irradiated particle (Fig. 6(a, b)). The O:C ratios on the gap side of the safety-tested particle (Fig. 7a) generally start around 1.25 and fall to about 0.5 with some additional scattered points, though the trend is approximately linear. In contrast, Fig. 6b shows that the O:C ratio begins near 2.5 and falls to around 0.2 with a curve more similar to an exponential function. Fig. 7(c, e, g, i) shows the 24 μm-thick KP on the particle's gap side while Fig. 7(d, f, h, j) shows the 60 μm-thick KP on the particle's non-gap side. In both cases the increased Sr content is coincident with decreasing O:C ratios. Although the safety-tested particle has generally higher O:C ratios in the KP than does the as-irradiated particle, Sr concentrations remain elevated in the KP of both particles, suggesting its preference for the carbide phase and additional radial transport as a result of the safety-testing.

The O:C ratios observed in the safety-tested particle at the outer edge of the inner kernel (Fig. 7a, b) are up to two times larger than those observed in the as-irradiated particle (Fig. 6a, b). In addition, O:C ratios in the safety-tested particle fall to a low of approximately 0.2–0.5 and do so more gradually than observed in the as-irradiated particle. This seems to be consistent with the fact that RT ln P_{O2} increases (becomes less negative) as the temperature increases, which occurs during safety-testing [37].

Finally, for both particles, the O:C ratio begins higher on the non-gap side of the particles than it does on the gap side of the particles; however, the ratio falls to a similar value regardless of whether there is a gap or not. The implications of these observations will be addressed in Sections 4.1 and 4.3–4.5.

3.4. Fission product whole particle mass balance calculations

Using the mass balance calculation process described in Section 2.4, the estimated FP mass per particle is shown in Table 2 along with the masses of select fission products in an average particle as computed by coupled Monte Carlo N-Particle (MCNP) and Oak Ridge Isotope Generation (ORIGEN) simulations. These simulations predicted the fission product inventory at the compact level based on the power history of the irradiation in ATR [26]. The elemental mass per particle listed in Table 2 is the inventory of an average particle in each of the two compacts, which was calculated by taking the total compact inventory and dividing by 3176, the average number of particles in each compact.

Electron probe microanalysis of U, La, Ce, Pr, Nd, Eu, Mo, Zr, Cs, I, and Pd are within ± 20% of their predicted values with EPMA values tending to overestimate compared to the predictions. Elements Sr, Sm, Ba and Ru show mixed results where one particle shows considerably better agreement than the other. The elements Xe, Te, and Ag do not show very good agreement between measured and predicted values. Because it is a gas, Xe is likely lost during sample preparation.

The ORIGEN-predicted quantities in Table 2 assume zero loss of any element from the particle. Therefore, elements such as Ag, Sr, and Eu, which are readily lost during irradiation, are overestimated. This suggests that the error implied by the fractional difference reported for Ag, Sr, and Eu is greater than it appears in Table 2.

Additionally, the inhomogeneous distribution of Ba, Te and Ag may result in larger errors when attempting to capture their variation with only two analyzed EPMA radial traverses.

3.5. Fission product distribution in safety-tested versus as-irradiated particles

Sections 3.2.1–3.3 provided data concerning differing FP, C and O concentration gradients in the safety-tested versus as-irradiated particles utilizing EPMA traverses across a plane to give a two-dimensional representation of the FP distribution. By employing the method described in Section 2.4, it is possible to approximate the total FP masses in different particle layers across three dimensions, thus arriving at both an estimated FP inventory for the whole particle (see Section 3.4) and the mass inventory for each particle layer. This allows a more thorough comparison of FP migration within the particle layers between the two particle treatments. With the exception of Ag, the TRISO layer elemental distributions presented are from those elements with reasonably good agreement between their measured and predicted masses.

Fig. 8(a, b) shows that greater than 78% of Cs and 71% of iodine have migrated outside the kernel and KP into the buffer and IPyC layers in as-irradiated particle AGR2-223-RS34. In contrast, safety-tested particle AGR2-222-RS19 contains 90% of its Cs mass and 96.6% of its iodine mass outside the kernel and KP. The slightly higher burnup of the safety-tested particle should create 13% more

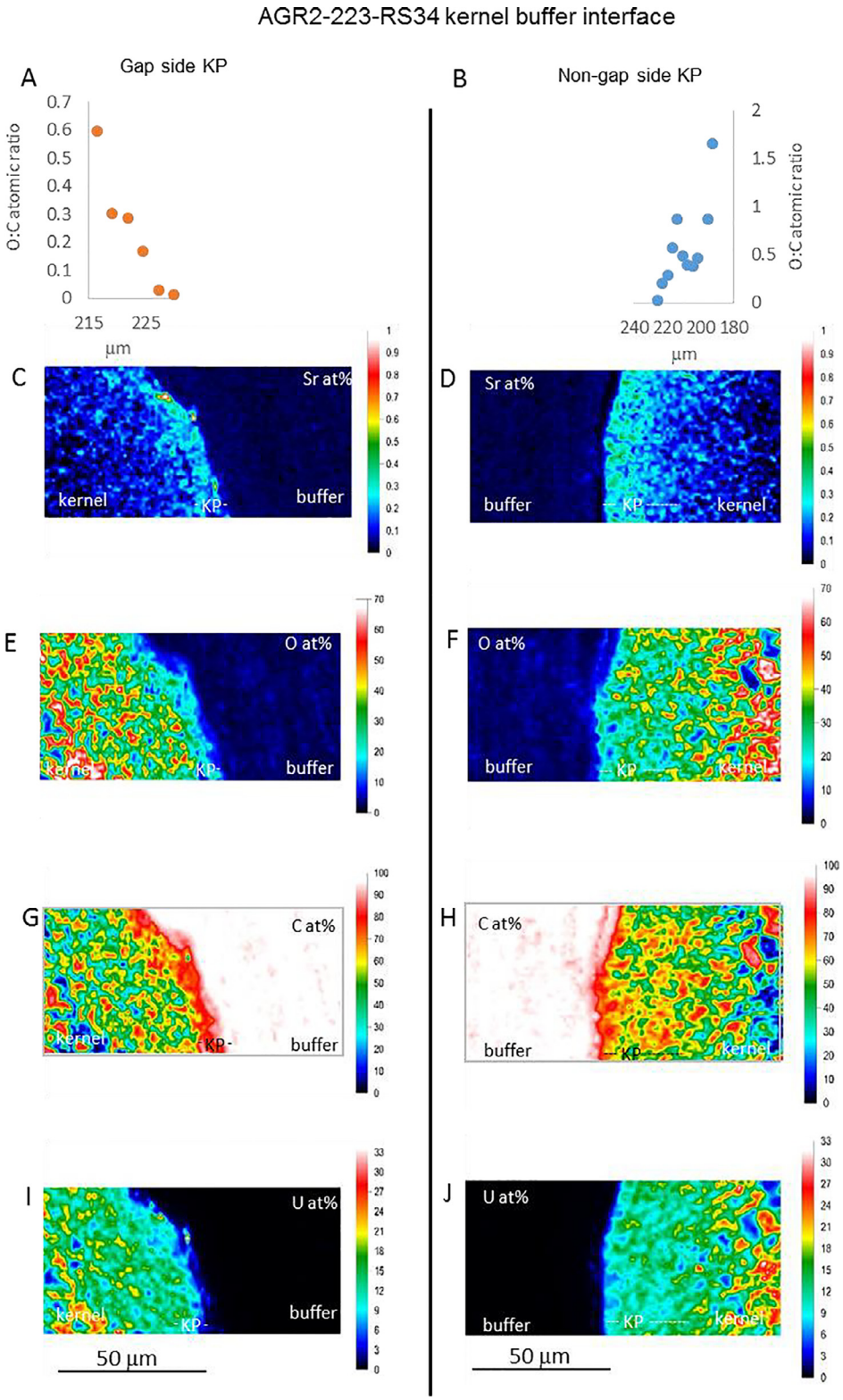

Fig. 6. (a–j). Quantitative X-ray maps of the kernel-buffer interface on the gap and non-gap side of as-irradiated AGR2-223-RS34. A and B show the O:C atomic ratio in the KP of both sides; C-D, E-F, G-H, I-J show quantitative X-ray maps of Sr, O, C, and U, respectively, in atomic% on the gap side (left column) and the non-gap side (right column). The KP, buffer, and kernel are shown on each X-ray map. The buffer is nearly 100% carbon, so it is shown in white with some pink on the carbon X-ray maps. (For interpretation of the references to colour in this figure legend, the reader is referred to the web version of this article.)

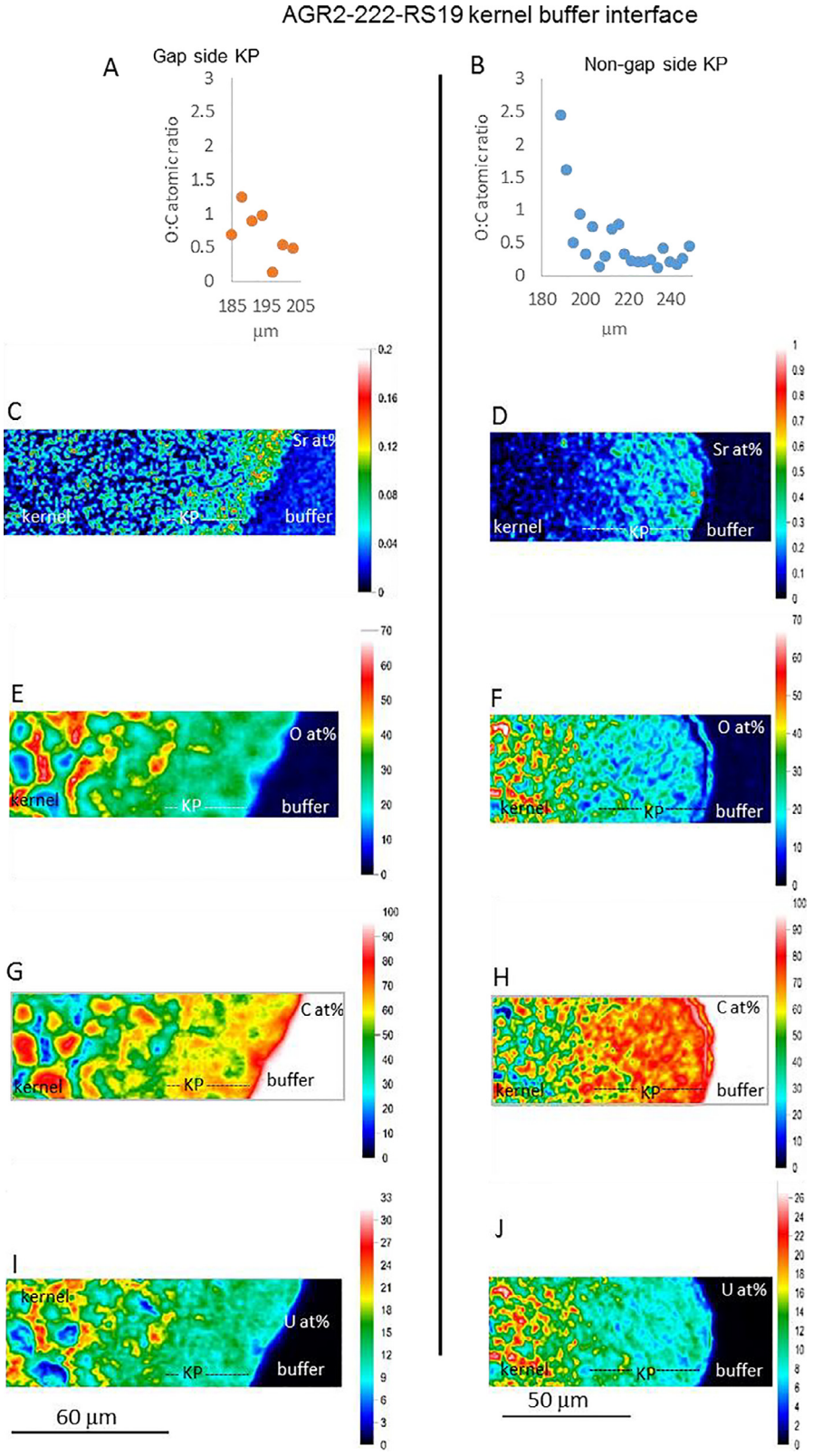

Fig. 7. (a–j). Shows quantitative X-ray maps of the kernel-buffer interface on the gap and non-gap side of irradiated and safety-tested AGR2-222-RS19. A and B show the O:C atomic ratio in the KP of both sides; C-D, E-F, G-H, I-J show quantitative X-ray maps of Sr, O, C, and U, respectively, in atomic% on the gap side (left column) and the non-gap side (right column). The KP, buffer, and kernel are shown on each X-ray map.

Table 2
Mass estimates of select FPs and U located in each particle, compared to the MCNP-ORIGEN calculations for those elements (masses in micrograms per particle). The fractional difference for each element is calculated as the ratio of the measured EPMA value divided by the ORIGEN-calculated value. Elements highlighted in green are within ± 20% of their predicted values. Elements highlighted in yellow are within 30% of their predicted values, and elements highlighted in pink deviate from their predicted values by > 30%.

Element, µg/particle	EPMA (AGR2-223-RS34)	Origen (AGR2-223-RS34)	fractional difference	EPMA (AGR2-222-RS19)	Origen (AGR2-222-RS19)	fractional difference
U	381	346	1.10	375	339	1.11
La	1.69	1.57	1.08	2.17	1.82	1.19
Ce	3.34	3.03	1.10	4.13	3.53	1.17
Pr	1.46	1.45	1.01	1.88	1.68	1.12
Nd	5.28	5.24	1.01	7.04	6.12	1.15
Sm	1.08	0.90	1.19	1.30	1.06	1.23
Eu	0.12	0.13	0.91	0.17	0.15	1.08
Mo	4.81	4.21	1.14	5.60	4.91	1.14
Ru	3.13	2.36	1.32	3.22	2.81	1.15
Zr	5.04	4.84	1.04	6.32	5.61	1.13
Xe	0.38	6.57	0.06	0.51	7.77	0.07
Cs	2.50	3.13	0.80	3.29	3.55	0.93
I	0.22	0.23	0.97	0.29	0.27	1.07
Ba	2.21	2.00	1.11	3.76	2.36	1.59
Sr	1.56	1.22	1.28	1.34	1.39	0.96
Te	1.27	0.52	2.45	2.51	0.61	4.13
Pd	0.80	0.99	0.81	1.13	1.29	0.88
Cd	0.01	0.06	0.17	0.02	0.07	0.24
Ag	0.07	0.05	1.41	0.11	0.07	1.62

Cs and 16% more iodine than is produced in the as-irradiated particle. Yet, the percentage of Cs and iodine in the safety-tested particle's buffer and IPyC is 19% higher for Cs and 35% higher for iodine, than is measured in the as-irradiated particle, which is greater than can be explained by burnup alone. This suggests that the higher irradiation temperature combined with very high temperature exposure during the safety test resulted in increased iodine and Cs transport radially outward.

Fig. 9(a, b) shows that the largest mass proportion of Sr and Eu is located in the KP for both particles. Similar Sr and Eu behavior is expected given that they have similar oxide-carbide equilibria; however, Sr in the KP is on the order of 50% higher in the safety-tested particle compared to the as-irradiated particle (Fig. 9a). Fig. 9b shows that Eu behavior in the kernel and KP appears similar to that observed with Sr; unfortunately, due to the large analytical error associated with measuring small quantities of Eu, the KP measurements show no statistical difference. However, due to the significantly larger number of points measured in each kernel, the non-parametric (due to failure of the Shapiro-Wilk normality test) Mann-Whitney Rank Sum Test was used to compare the median kernel masses of Eu measured in each particle. This test showed a statistically significant difference in the Eu median masses, with the kernel of as-irradiated AGR2-223-RS34 having a larger Eu median mass than safety-tested particle AGR2-222-RS19, which is what is observed in Fig. 9b. This suggests that the trends observed in Fig. 9b may be similar to those observed with Sr in Fig. 9a, but these results should be interpreted cautiously. If these Eu and Sr trends remain similar with further investigation, such behavior may be attributable to enhanced radial transport resulting from safety testing.

Fig. 10(a, b) shows distinctively different behaviors between the safety-tested particle and the as-irradiated particle for elements

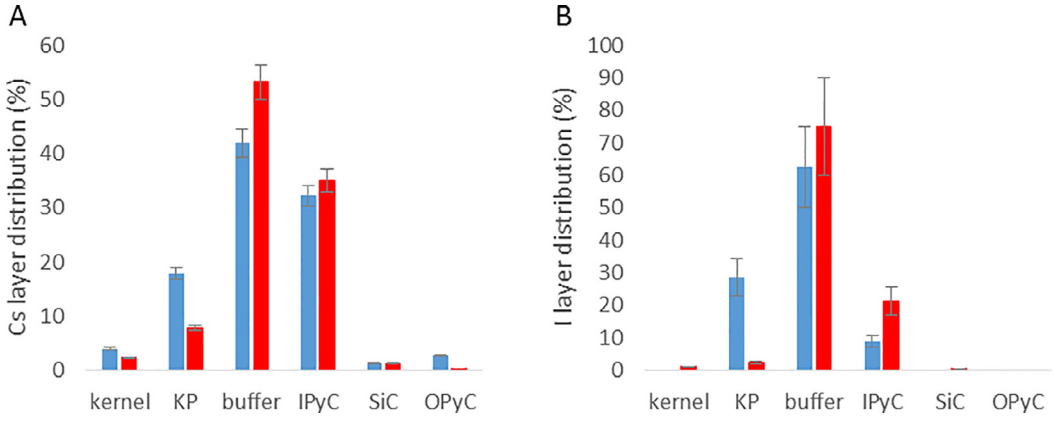

Fig. 8. (a, b). Shows Cs and I total elemental mass proportion (%) and distribution within safety-tested particle AGR2-222-RS19 (red) and as-irradiated particle AGR2-223-RS34 (blue). (For interpretation of the references to colour in this figure legend, the reader is referred to the web version of this article.)

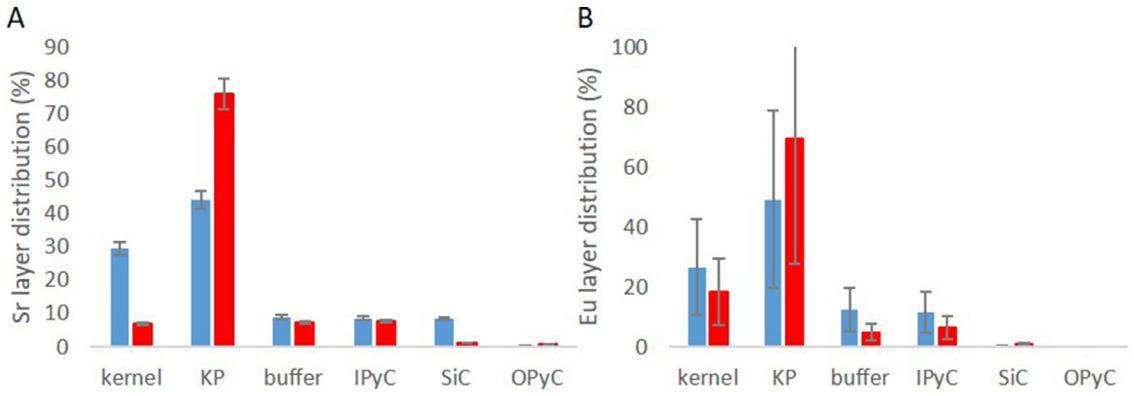

Fig. 9. (a, b). Shows Sr and Eu total elemental mass proportion (%) and distribution within safety-tested particle AGR2-222-RS19 (red) and as-irradiated particle AGR2-223-RS34 (blue). (For interpretation of the references to colour in this figure legend, the reader is referred to the web version of this article.)

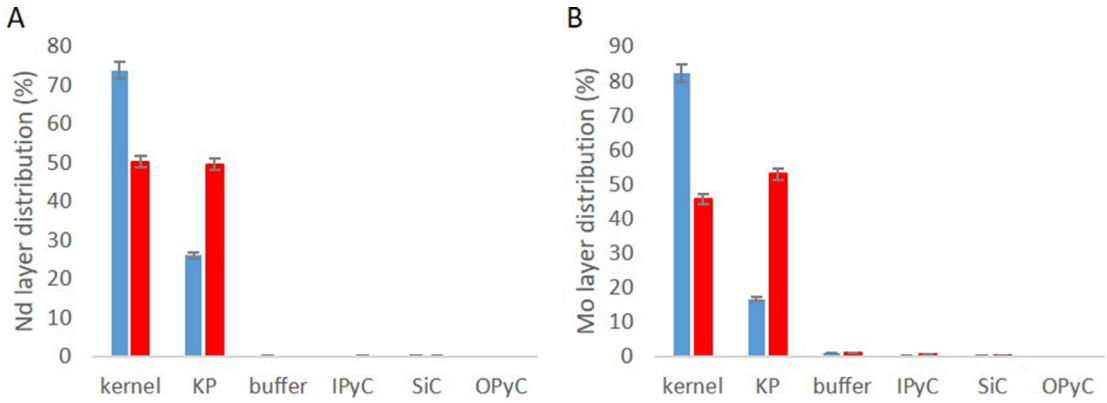

Fig. 10. (a, b). Shows Nd and Mo total elemental mass proportion (%) and distribution within safety-tested particle AGR2–222-RS19 (red) and as-irradiated particle AGR2–223-RS34 (blue). (For interpretation of the references to colour in this figure legend, the reader is referred to the web version of this article.)

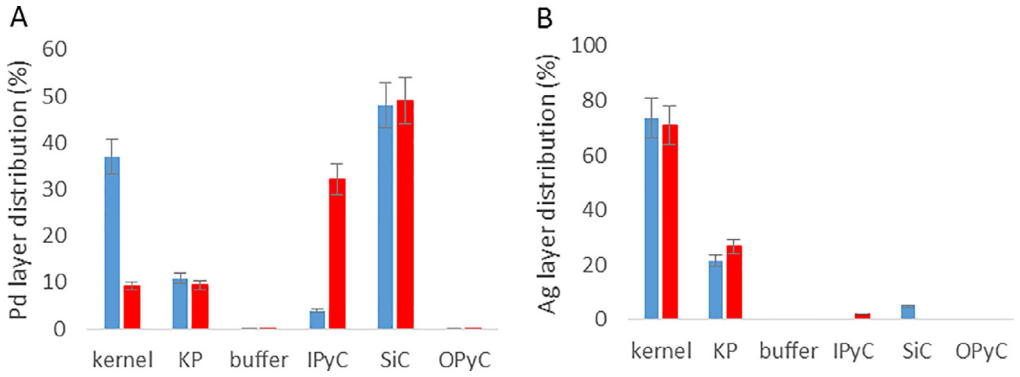

Fig. 11. (a, b). Shows Pd and Ag total elemental mass proportion (%) and distribution within safety-tested particle AGR2-222-RS19 (red) and as-irradiated particle AGR2-223-RS34 (blue). (For interpretation of the references to colour in this figure legend, the reader is referred to the web version of this article.)

Nd and Mo. In the safety-tested particle, Nd is equally divided between the kernel and KP while Mo is slightly more abundant in the KP. In the as-irradiated particle, three times more Nd mass and five times more Mo mass remains in the inner kernel. Similar behavior occurs with Ru and lanthanide elements, with the exception of Eu, which behaves like Sr.

Palladium and Ag behavior is of interest because the elements tend to be found together at the IPyC-SiC interface [38,39]. Additionally, Ag release from TRISO particles is a safety concern during maintenance, because the released Ag tends to condense onto the cooler turbine blades. Fig. 11a shows that with regard to Pd, the safety-tested particle contains roughly equal amounts of Pd in the kernel and KP, with approximately three times more in the IPyC and five times more detected in the SiC than was measured in the kernel. In contrast, Pd in the as-irradiated particle occurs in large quantities in the kernel and SiC, but only 4% of the Pd in that particle is present in the IPyC. Neither particle retains much Pd in the buffer. It appears to transport directly though the buffer to accumulate in the IPyC and SiC. Additionally, the safety-tested particle shows that the increased heat and time involved with the safety test appears to result in higher quantities of Pd transporting further away from the kernel. Silver behavior is similar for both particles (Fig. 11b). In both particles, the largest quantity remaining in the particles is located in the kernel with about 60% less located in the KP. A small mass is located in the IPyC of the safety-tested particle and in the SiC of the as-irradiated particle.

Silver and Pd behave quite differently from one another, regardless of whether the particle has been safety tested or not. Pd is

detected in low, but relatively constant concentrations occurring throughout the kernel and KP of both particles. In the as-irradiated particle, 48% of the Pd mass is retained in the kernel and KP, whereas in the safety-tested particle, 19% is retained in the kernel and KP—demonstrating that safety testing results in enhanced radial transport outward. In contrast, silver occurs as low (i.e. 200–2000 ppm), isolated concentrations located sporadically through the kernel and the KP of both particles. It does not collect in the buffer, but resumes accumulation in the IPyC and SiC. Silver can transport significantly through intact TRISO coatings, and gamma counting prior to microscopy showed that as-irradiated particle AGR2-223-RS34 and safety-tested particle AGR2-222-RS19 retained 84% and 20% of the ^{110m}Ag inventory predicted in an average particle, respectively. Thus, in the safety-tested particle very little Ag actually remained in the particle, and the silver that did remain was localized primarily in the kernel and KP. Because this method assumes reasonable symmetry to achieve mass balance closure, asymmetrical Ag distribution results in EPMA silver mass balance over-estimation by 40–60% compared to the MCNP-ORIGEN calculations, which have not been adjusted for Ag loss.

4. Discussion

4.1. Particle morphology and fission product distribution

For both Particles AGR2-222-RS19 and AGR2-223-RS34, two radial traverses were examined, one on the side of the particle where the buffer remained bonded to the IPyC, and one on the side where the buffer became delaminated from the IPyC, creating a substantial gap between the buffer and IPyC. This morphology is quite common among irradiated AGR-1 and AGR-2 particles and is thought to be the result of the inward buffer densification [40–42].

Fig. 3 shows that Cs has crossed the gap and appears to maintain a similar concentration profile to the profile on the gap-less side of the particle. Iodine had a similar profile. This suggests that the gap formed after Cs and I had migrated into the IPyC, or that the gap did not significantly alter the transport properties of these elements. The latter seems more likely because these fission products would have been continually produced throughout the irradiation.

While most FPs have similar concentration profiles on both sides of the particle (gap side versus non-gap side), Sr, Te, Ba, and to a lesser extent, Eu do not. Strontium concentrations are up to five times higher in the KP of the non-gap side of safety-tested particle than on the side with the gap (Fig. 4(a, b)), with Te, Ba, and Eu behaving similarly (data not shown). This difference cannot be due to the void space resulting from gap formation, as the gap is beyond the buffer, outside of this concentration spike; however, the gap's presence can affect temperature as will be demonstrated in Section 4.6.

4.2. Comparison with other works

To the authors' knowledge, this work is the first to characterize such a large number of fission products on a layer-by-layer basis in irradiated and safety-tested AGR-2 particles; however, Gerczak et al. [22] used scanning electron microscopy with energy dispersive spectroscopy (SEM-EDS) to examine a large number of irradiated and safety-tested AGR-2 particles with particular attention to high-Z feature composition near the IPyC-SiC boundary and into the SiC layer. Gerczak et al. [22] specifically examined particle AGR2-223-RS34. While they did not examine safety-tested particle AGR2-222-RS19, they did examine particles from safety-tested compact 6-4-2.

Some salient findings for as-irradiated AGR2-223-RS34 include the following:

- High-Z features were found throughout the layers.
- High-Z features accumulated along the IPyC-SiC boundary for the entire circumference of the particle.
- High-Z features along the IPyC-SiC interface were composed predominantly of Pd-U or U-Zr-Pd.
- High-Z features within the SiC were composed of Pd-U or Pd only as the OPyC layer was approached.
- As a particle that retained most of its Ag, AGR2-223-RS34 appeared to have a lower U content in U-bearing features compared to particles that did not retain much Ag inventory.

For particles examined from safety-tested compact 6-4-2, findings include the following:

- High-Z features at the IPyC-SiC boundary were predominantly Pd-U.
- For low Ag-retaining particles, high-Z features located within the first 5 μm of the IPyC-SiC boundary were predominantly Pd-U, whereas high-Z features located > 5 μm from the boundary were predominantly Pd-only.
- Other features in the SiC layer of low Ag-retaining particles were predominantly U-Zr and U-Pd.

Comparing Gerczak et al. [22] work to this work is complicated. While the former work focused on high-Z features in the IPyC and SiC, this work is concerned with radial concentration profiles of a large number of fission products across two particles. For this work, a 20 keV accelerating voltage was used to increase X-ray counts from minor and trace elements. As a consequence, in the IPyC region, the beam interaction volume is approximately 3 μm while it is approximately 2 μm in the SiC layer. Because the high-Z features tend to be much smaller than the beam volume [43], EPMA point measurements may encompass one or more high-Z features. This is most to occur likely near the IPyC-SiC interface as the features are more abundant at this location. Additionally, in the SiC layer precipitates tend to be found along grain boundaries [36]. Because the SiC grains are smaller than the EPMA beam interaction volume, such precipitates may be included with the SiC matrix while measuring points in the SiC layer.

Despite these caveats, comparisons can be made between the findings of Gerczak et al. [22] and those from this work.

In the IPyC of both sides of the the as-irradiated particle, U tends to dominate Pd, Zr, Mo, and Ru, while in the SiC layer, Pd dominates U, Zr, Mo, and Ru. Ag is found in the first 2 μm of the SiC on the non-gap side only (Fig. 5(a-d)).

In the SiC of the as-irradiated particle, on the non-gap side Pd > U > Zr > Mo > Ru. U, Zr and Mo are not detected in the SiC layer on the gap side of the particle (Fig. 5(b, d)).

Gerczak et al. [22] noted Pd-U and U-Zr-Pd features on the IPyC side of the IPyC-SiC interface and Pd-U and Pd-only phases in the SiC layer, which appears consistent with the findings of this work.

In the IPyC of both sides of the safety-tested particle, U dominates Pd, Zr, Mo, and Ru until the IPyC-SiC boundary is approached where Pd > U > Zr ≅ Mo > Ag > Ru (Fig. 5(e-h)). On the gap side Ag is not detected (Fig. 5g).

In the SiC of the safety-tested particle, Pd dominates U, Zr, Mo, and Zr with the latter four elements not detected beyond 10 μm into the SiC layer on the gap side, though Zr and Cs are detected sporadically in the SiC layer on the non-gap side (Fig. 5(f, h)).

These findings are also consistent with those of Gerczak et al. [22] who noted Pd-U features near the IPyC-SiC boundary and into the SiC layer, with Pd-only features found beyond 5 μm into the SiC layer. Gerczak et al. [22] also hypothesize that greater U presence correlates with higher temperature samples. As U is more abundant in the IPyC and SiC of the safety-tested particle, this work is consistent with the findings of Gerczak et al. [22].

While EDS spectra from Gerzak et al. [22] contained Cs and Ba peaks, they appear to comprise minor constituents compared to

Pd, U, and Zr, whereas in this work, Ba and Cs appear much more abundant, suggesting that these elements may be more concentrated in the surrounding matrix than in the high-Z features.

4.3. Temperature effects

Several researchers describe the effects of temperature gradients across TRISO particles. Tiegs [13] and Minato et al. [14] both describe the transport of Pd and rare earth elements down the temperature gradient. Grubmeier et al. [44] noted the diffusion of rare earth and platinum group elements to the cooler side of the particle but stated that they were not necessarily co-located. Kleykamp [12] described the presence of an "azimuthal temperature gradient" across the particle that influenced FP transport and precipitation.

Fig. 5(a, b) shows that for both particles, Pd is as much as 10 times higher in concentration on the non-gap side than on the side with the gap. Silver is detected only on the non-gap side of these two particles (Fig. 5(a, e)). Fig. 1 (a, b, boxes 1 and 2) shows visible precipitates at the IPyC-SiC interface, whereas no such obvious precipitates are present at the IPyC-SiC interface where the buffer has been separated substantially from the IPyC.

Kleykamp [12] showed that for TRISO with UO_2 kernels, Te and Pd migrated to the cold side of the particle. In this study with UCO particles, Te, Sr, Ba, and Eu all exhibit similar behavior, and Sr, Ba, and Eu are predicted to exist as carbides [37]. Carbides are more mobile than oxides, and tend to move radially farther out from the center of the oxygen-rich kernel than the oxides. This is likely why elements such as Sr, Ba, and Eu reside preferentially in the KP (Figs. 6, 7), which is much more carbon-rich than the inner kernel. While Te concentration gradients in the KP are similar to those of Sr, Ba, and Eu, the Te accumulation mechanism is likely different from those elements. Minato et al. [14] noted the presence of elemental Te while other researchers describe Te existing as an inter-metallic compound [45]. Given that the precipitates are located primarily on the non-gap side of the particles, which is also is enriched in Sr, Te, Ba, and Eu, this suggests that this side of both particles is relatively carbon-rich and may also be the cooler than the gap-side of both particles. Buffer creep deformation is enhanced at higher temperatures [40,46] which may promote gap formation on the hotter side of the particle and no (or a smaller) gap on the cooler side. Alternatively, it is possible that Pd and Ag transport on the gap-side of the particle is impeded by the gap's presence.

Mechanisms for intra-particle temperature differences and gradients will be discussed in Section 4.4.

4.4. BISON modeling

BISON [47] is a nuclear fuel performance code that is capable of modeling multiple fuels in a wide variety of dimensions and geometries. For TRISO fuel, BISON-developed thermo-mechanical models [48,49] for each material layer include elastic, irradiation creep, irradiation-induced dimension change, thermal expansion and thermal conductivity. The thermo-mechanical behaviors of AGR-2 compacts 2-2-2 and 2-2-3 were simulated with BISON. Their irradiation conditions and fuel properties are provided in Tables 1 and 3, respectively. BISON models use time-average, volume-averaged compact daily temperatures as boundary conditions at the outer edge of the OPyC layer. BISON calculates the temperature profile between the kernel center and the OPyC layer. In the first case, the buffer and IPyC layer are fully bonded, and the temperature profile is continuous from the buffer to the IPyC layer. In the second case, a gap is formed between the buffer and IPyC layer, and the temperature profile is affected by the width of the gap. The heat transfer through the buffer-IPyC gap is modeled with a gap conductance model. Temperature profiles with and without the buffer-IPyC gap of Compact 2-2-3 and 2-2-2 at the end of the irradiation are shown in Fig. 12(a, b). The temperature at the buffer is about 15–20 °C higher than the IPyC layer with the gap between the buffer and IPyC while the temperature is continuous without the gap.

Table 3
Parameters used in modeling the AGR-2 irradiation [1–8].

Category	Parameter	Value
Fuel Characteristics	235 U enrichment (wt%)	14.029
	Carbon/uranium (atomic ratio)	0.392
	Oxygen/uranium (atomic ratio)	1.428
Particle geometry	Kernel diameter (μm)	426.7
	Buffer thickness (μm)	98.9
	IPyC (μm)	40.4
	SiC thickness (μm)	35.2
	OPyC thickness (μm)	43.4
Pre-irradiation fuel properties	Kernel density (g/cm^3)	10.966
	Kernel theoretical density (g/cm^3)	11.37
	Buffer density(g/cm^3)	1.05
	Buffer theoretical density (g/cm^3)	2.25
	IPyC density (g/cm^3)	1.89
	OPyC density(g/cm^3)	1.907
	IPyC Bacon Anisotropy Factor (BAF)	1.0465
	OPyC BAF	1.0429

The TAVA temperatures used in this model are representative of an average particle in the compact located near the centerline, with no thermal gradient and the subsequent temperature gradient across the particle caused by gap formation. A particle located near the compact exterior surface will exist in a temperature gradient prior to gap formation that may be larger than the 15–20 °C modeled here. While the 3-D spatial location of either particle in their respective compact is unknown, the model demonstrates that the gap side of the particle is hotter than the non-gap side, and that there is a temperature gradient change across the radius when the gap is encountered. The gap might form in response to elevated temperature; however, some particles have a gap on more than one side of the exposed plane, making it unlikely that there is a "hot" side of the particle that contributes to gap formation. Moreover, there is little to no thermal gradient during a safety test, but the temperature is elevated several hundred degrees above its irradiation temperature. If gap formation was due to elevated temperature alone, safety-tested particles would tend to have extensive buffer delamination, but such behavior has not been observed. More likely, the gap forms during irradiation due to inward buffer densification, which tends to be asymmetrical. Once the gap is formed, that side of particle becomes hotter than the gap-less side because thermal conductivity is improved when the layers are not interrupted by a gas-filled gap.

Thus the cooler side of the particle does appear to coincide with the gap-less side of the particle when a gap is present in the particle.

4.5. Kernel periphery

Because of the tendency of some fission products to migrate preferentially to the KP, it is useful to examine some of the properties of this region of the particles. As mentioned in Section 1, the KP is the outer perimeter region of the kernel in which the U concentration drops rapidly while the C concentration increases to 100% where it meets the buffer. In this study, the KP varies from approximately 13–31 μm in thickness in particle AGR2-223-RS34, and 24–60 μm in thickness in particle AGR2-222-RS19. The

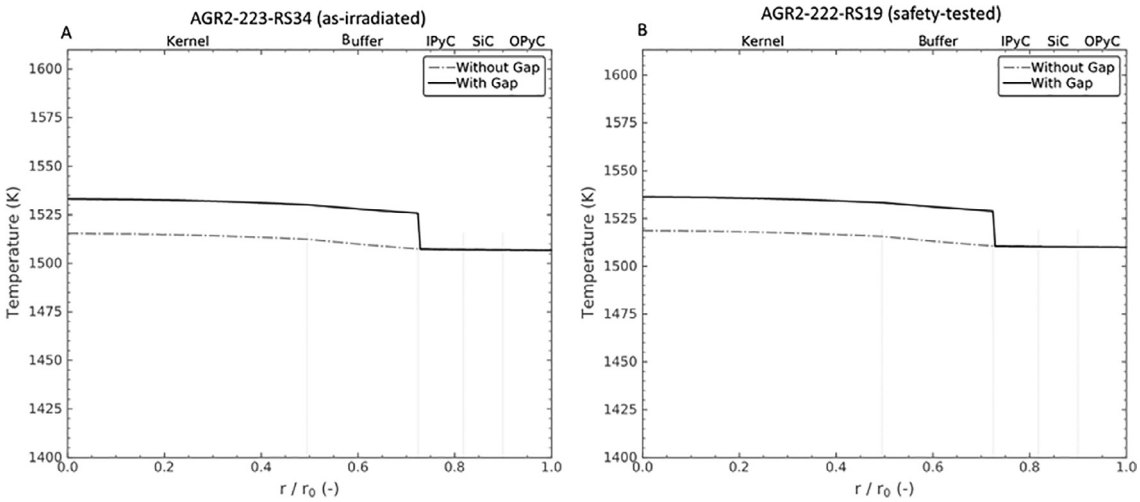

Fig. 12. (a, b). Shows BISON-predicted temperature gradients on the gap and non-gap sides of as-irradiated particle AGR2-223-RS34 (a); and safety-tested particle AGR2-222-RS19 (b).

Table 4
KP thicknesses in micrometers for AGR-2 particles examined by EPMA.

Particle	Gap Side of Particle (μm)	Non-Gap Side of Particle (μm)
*AGR2-223-RS34	13	31
#AGR2-223-RS06	21	23
*AGR2-222-RS19	24	60
#AGR2-222-RS27	15	42
#AGR2-633-RS28	14	27
#AGR2-633-RS09	21	28

*this study.
(van Rooyen et al., [25]).

KP forms when the particles are fabricated, but remains present during irradiation, and appears to influence FP accumulation as it becomes more carbon-rich during irradiation [25]. The KP varies in thickness not only in these two examined particles, but in other AGR-2 particles examined by EPMA (Table 4). While few particles have been examined, all share common features in that the KP region is narrower on the side of the particle with the buffer delamination (gap side) than it is on the side with no buffer delamination (non-gap side, Table 4). The thicker side is typically on the order of two times thicker than the thinner side. It is not clear whether the KP has such large thickness variations upon fabrication or whether asymmetrical thinning or thickening occurs during irradiation. Regardless, on the thicker KP side of the particle, elements such as Sr, Ba, Te, and Eu are found in higher concentrations compared to what is observed on the thinner KP side of the particle (Figs. 4, 6, 7; data not shown for Ba, Te, or Eu). This thicker side of the KP is more carbon-rich than other parts of the KP and coincides with what was modeled in the previous section to be the cooler side of the particle.

Section 3.3 described the observation that Sr, Ba, Eu, and Te concentrations increased greatly in the KP of both particles, and that this concentration increase is spatially correlated with low O:C ratios. Recent transmission electron microscopy (TEM) data made available in a report by van Rooyen et al. [25] shows that the irradiated KP is composed largely of UO_2 with sub-micrometer islands of amorphous carbon that appear to grow more abundant closer to the buffer. This increasing carbon at the expense of UO_2 appears in the EPMA data as increasing C with decreasing U and O as the buffer is approached. Because the EPMA's beam interaction volume ($\sim$1 μm^3) in the KP is much larger than the resolution of the TEM measurements of the same area, these compositional changes are seen as gradual.

Because Ba, Sr, and Eu are predicted to exist as carbides [37] their accumulation in a low O:C region is thermodynamically consistent. While the O:C ratio in the safety-tested particle is approximately two-times larger than measured in the as-irradiated particle, it remains sufficiently low to permit Ba, Sr, and Eu accumulation, presumably as carbides. While Te behaves similarly, it is not thermodynamically stable as a carbide and likely transported as a gas. At room temperature it likely exists elementally or as an inter-metallic with Pd [45]. More investigation is required to better understand Te behavior.

The large Ba, Sr, Eu, and Te concentrations observed on the non-gap side of the safety-tested particle may reflect kinetics. Because that KP location is so much thicker than the measured KP on either side of the as-irradiated particle or on the gap side of the safety-tested particle, there is a much thicker low oxygen potential (μO_2) region where reduction reactions can occur. Thus, given similar elemental transport rates on each side of the particle, more Ba, Sr, Eu, and Te will accumulate on the side with the thicker KP due to greater contact time in the chemically reducing area. Note that while C and O measurements are not yet accurate enough to extrapolate quantitative μO_2 data, they are sufficiently precise so as to permit direct comparison between the various regions of each particle and between the two particles.

4.6. Effect of safety testing on fission product distribution

As seen in Figs. 8–11, this study suggests that safety testing appears to have an impact on the fission product distribution in the particle. For almost all measured elements, the fission product mass in a particular layer (outside the kernel) of the safety-tested particle is either higher than that in the analogous layer of the as-irradiated particle, or the mass in the safety-tested particle is detected further away from the kernel than in the as-irradiated particle, or both. This suggests that the elevated temperature of the safety test (1600°) or the higher irradiation temperature in the safety-tested particles promotes noticeable FP transport in the particle, allowing less mobile elements such as lanthanides, Mo, and Zr to be detected further away from the kernel of the safety-tested particle compared to the as-irradiated particle.

Without separate-effects testing, it is difficult to distinguish between effects due to 1600 °C post-irradiation safety testing and those purely from irradiation. This is partly due to the difference in irradiation temperature between Compact 2-2-3 (TAVA=1261 °C) and safety-tested Compact 2-2-2 (TAVA=1287 °C). As described in Section 2.1, the maximum possible temperature difference between

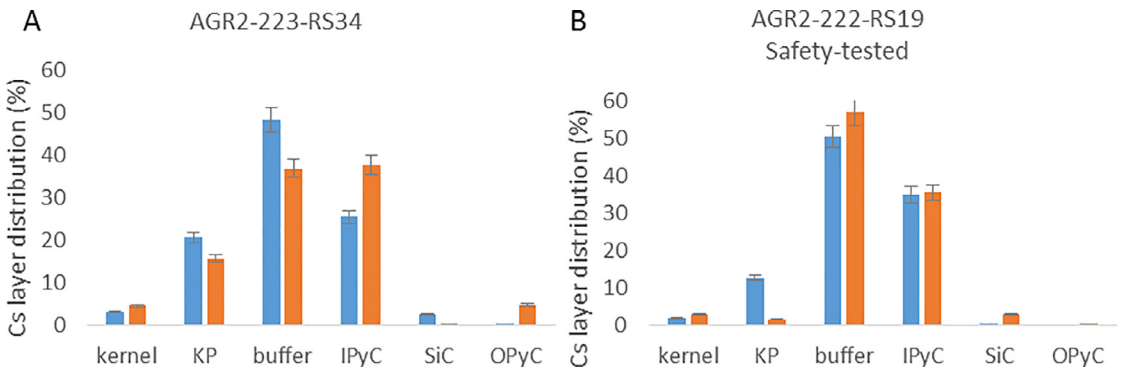

Fig. 13. (a, b). Shows Cs elemental proportion (%) and distribution within as-irradiated particle AGR2-223-RS34 and safety-tested particle AGR2-222-RS19 for both measured halves of each particle. The non-gap side is shown in blue and the gap side is shown in orange. (For interpretation of the references to colour in this figure legend, the reader is referred to the web version of this article.)

the two particles is 193 °C, though the actual difference may be smaller.

However, additional data provide some clues. Similar to interpreting Nd and Mo transport in safety-tested particles and non-safety-tested particles, it is possible to see some differences in Cs transport that cannot be wholly explained by irradiation temperature differences. van Rooyen et al. [25] showed that safety-tested AGR-1 particles that had been irradiated at 1094 °C (167 °C lower than the TAVA irradiation temperature of as-irradiated AGR2-223-RS34) led to very little Cs-retention in the AGR-1 particles, suggesting that the higher temperatures imparted through safety-testing have a much larger influence over FP distribution than the smaller irradiation temperature differences.

As seen in Figs. 3 and 4, it is possible to plot the measured elemental concentration across the two measured radial traverses for each particle. However, it is also useful to apply the mass balance calculation method described in Section 2.4 to determine the actual elemental mass in each particle layer for both halves of the particle. As described in Sections 4.1, 4.2, and 4.5, some elements, such as Sr, are not symmetrically distributed laterally across the particles, whereas other elements, such as Cs, are somewhat more evenly distributed. Fig. 13 shows the Cs elemental distribution across both halves of both examined particles. Fig. 13a shows that for both sides of the as-irradiated particle, approximately the same proportion of Cs (~20–24%) remains in the kernel and KP. On the non-gap side the buffer contains approximately twice as much Cs as was measured in the IPyC; whereas on the gap-side, Cs is spread evenly between the buffer and IPyC, and the OPyC contains approximately ten-fold more Cs than is found in the non-gap side of the particle. Fig. 13b shows that for the safety-tested particle, 85–92% is located in the buffer and IPyC on both sides, but like the non-safety tested-particle, a larger proportion of Cs is located in the OPyC on the gap side of the particle than on the gap-less side of the particle. These observations suggest that for both studied particles, Cs travels farther from the kernel on the side with the gap.

Fig. 14(a, b) shows the Sr percent elemental distribution for both halves of both particles. For as-irradiated particle AGR2-223-RS34, the proportion of Sr in the KP on the non-gap side of the particle is about 50% greater than the proportion present in the KP on the gap side of the particle. Additionally, on the non-gap side, the largest Sr proportion is found in the KP, whereas on the gap side the greatest Sr proportion is divided approximately equally between the KP and kernel. For safety-tested particle AGR2-222-RS19, the Sr proportion in the KP on the non-gap side is approximately twice that on the gap side of the particle, and unlike the as-irradiated particle, the vast majority of the Sr mass (83%) is located in the KP on the non-gap side.

Fig. 15(a, d) shows Pd and Ag distribution among the particle layers on both sides and in both particles. In as-irradiated particle AGR2-223-RS34, the Pd mass in the SiC layer on the non-gap side is roughly twice that measured on the side with the gap (Fig. 15a). The Pd mass distribution in safety-tested particle AGR2-222-RS19 shows that more than twice as much Pd mass is found on the non-gap side compared to the side with the gap (Fig. 15b). For both particles, silver is detected further away from the particles' center on the non-gap side compared to the side with the gap, where Ag is not observed beyond the KP on the gap side of the as-irradiated particle nor beyond the kernel on the gap side of the safety-tested particle (Fig. 15(c, d)).

The lateral behavioral transport differences between Cs, Sr, Pd and Ag suggest that there is something fundamental about the gap side versus the non-gap side of these particles that influences FP transport. There are several possibilities to explain this including: (1) the non-gap side's thicker KP provides increased volume of lower μO_2 region, which then promotes accumulation of carbide phases containing Sr, Eu, or Ba; (2) gap formation itself facilitates transport of particularly volatile elements such as I and Cs because the void created does not have the surface area that the buffer has, thus transport is unconstrained until the IPyC is encountered; (3) elements such as Sr, Te, Eu, and Ba form in a roughly equal distribution within the kernel, but the growing KP thickness promotes element redistribution whereby these elements are preferentially retained in the thicker KP; and (4) the plausible temperature gradient difference suggesting that the non-gap side is cooler than the gap side promotes fission product diffusion to the cool side of the particle (e.g. Grubmeier et al. [44]). It is possible that more than one of these mechanisms occurs. More data are needed to test these hypotheses.

4.7. Mass balance accuracy and opportunities for future work

As noted in Section 3.4, some EPMA-calculated element masses compare very well to the MCNP-ORIGEN-model predictions, while others diverge substantially. Uranium was measured by EPMA not because of specific interest in its distribution, but to compare the EPMA mass-calculation method with the ORIGEN-modeled calculation using an element that was abundant (therefore having low measurement error) and was likely to stay primarily in the kernel. For both particles, the EPMA-measured U mass was within 11% of the ORIGEN-predicted mass. Other elements that compared favorably include Cs, Pd, I, La, Ce, Pr, Nd, Eu, Mo, and Zr.

Elements with moderate errors (20% > error ≤ 30%) include Sr and Sm. Elements with large (> 30%) errors include Ru, Xe, Ba, Te, and Ag. It is not completely clear why some EPMA-measured masses are more accurate than others. In some cases, there are an-

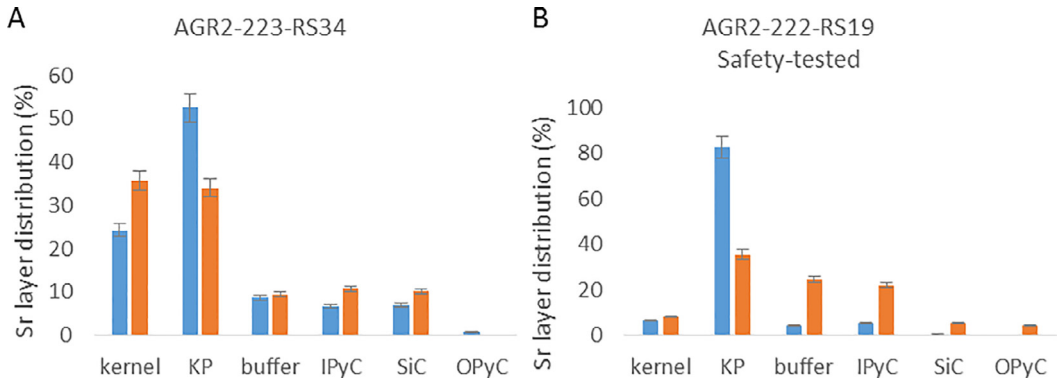

Fig. 14. (a, b). Shows Sr elemental mass proportion (%) and distribution within as-irradiated particle AGR2-223-RS34 and safety-tested particle AGR2-222-RS19 for both measured halves of each particle. The non-gap side is shown in blue and the gap side is shown in orange. (For interpretation of the references to colour in this figure legend, the reader is referred to the web version of this article.)

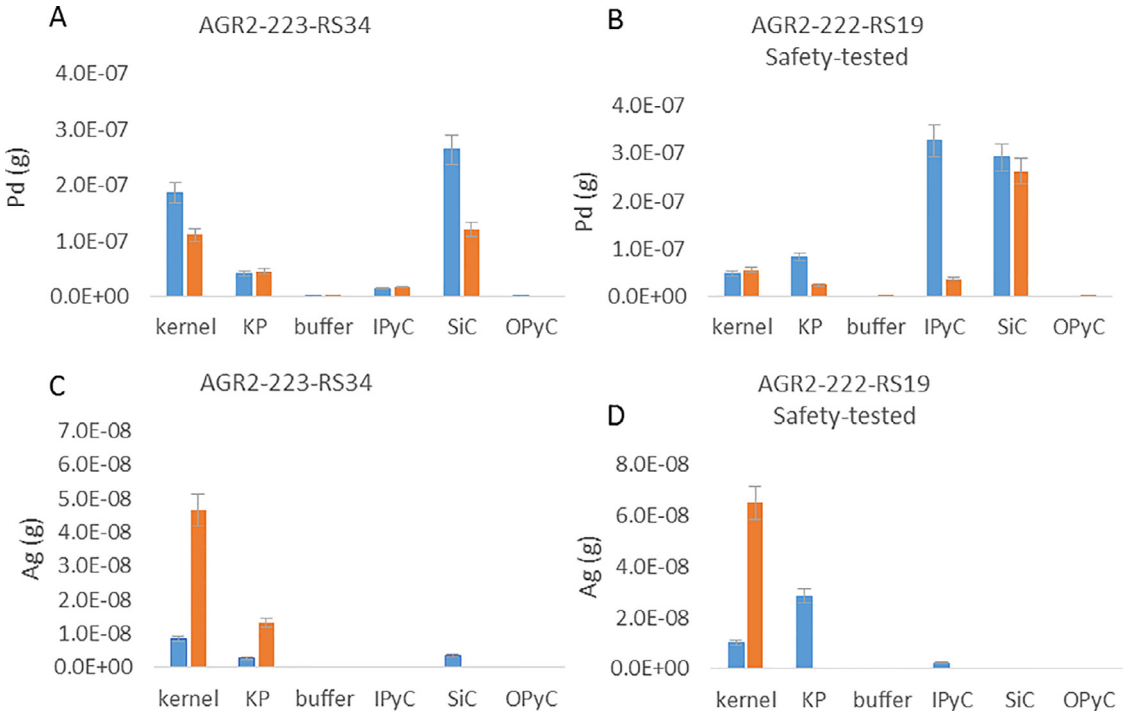

Fig. 15. (a, d). Shows Pd mass and distribution within as-irradiated particle AGR2-223-RS34 (a) and safety-tested particle AGR2-222-RS19 (b) for both measured halves of each particle. Ag mass and distribution within as-irradiated particle AGR2-223-RS34 is shown in (c) and safety-tested particle AGR2-222-RS19 is shown in (d) for both measured halves of each particle. The non-gap side is shown in blue and the gap side is shown in orange. (For interpretation of the references to colour in this figure legend, the reader is referred to the web version of this article.)

alytical difficulties. For example, accurately quantifying ~100 ppm-levels of Ag in a U matrix is difficult. Major U overlaps exist with the measured Ag Lβ analytical line. Because Ag is found in very small quantities relative to the overlapping peaks, peak deconvolutions may not be accurate. It is also possible that inhomogeneously distributed elements are more difficult to quantify accurately with only two radial traverses. Finally, it is possible that calibration standards are not accurate. To evaluate this possibility, the calibration standards were compared with single-element standards to confirm their accuracy, with no discrepancies identified.

Since this EPMA-measured mass method employed measurement of two radii, quantification can be improved by measuring additional radii in an attempt to capture the variability exhibited by the more inhomogenously distributed elements. Another possible way to capture the inhomogeneity would be to quantitatively X-ray map the elemental distribution of the exposed mid-plane surface and to extrapolate these concentrations to three dimensions.

5. Conclusion

The ensuing summary statements reflect analyses performed on two radial traverses on one as-irradiated TRISO particle and one irradiated and safety-tested particle. Because of the large number of particles per compact compared to the small number of analyzed particles, these conclusions represent analyses performed on the two particles studied in this work and should not be generalized to other un-analyzed particles. In addition, as only two radii per particle were measured, it is possible that these findings might not be replicated with other potential radii.

- For both particles, most of the mass of the following elements is located in the kernel and KP: Ru, Mo, Zr, Sr, Te, Eu, Ag, La, Ce,

Pr, and Sm. The majority of the Cs, I, Xe, and Pd mass was located in the particle coatings. Caution should be used interpreting Ag mass distribution as the mass balance was poor, likely due to heterogeneous elemental distribution and larger errors concomitant with low concentrations in a U matrix.

- In the safety-tested particle, Sr, Te, Ba, and Eu are up to five times higher in concentration in the KP on the non-gap side compared to the KP on the gap side.
- Pd and Ag are notably higher in concentration on the non-gap side of the IPyC-SiC boundary of both the safety-tested and as-irradiated particle.
- BISON modeling demonstrates that the kernel, KP, and buffer on gap side of both particles are 15–20 °C hotter than the kernel, KP, and buffer on the non-gap side of the particles. Such a temperature gradient would drive more mobile fission products to the cool side of the particle.
- Along the studied radial traverses, FPs such as Cs, I, Te, Sr, Ba, Ru, rare earth elements, Mo, and Pd, move out further from the particle center in the safety-tested particle than the as-irradiated particle; these data suggest that safety-testing may result in additional transport that cannot be accounted for by higher irradiation temperatures alone.
- The low O:C ratio in the KP likely favors Sr, Ba, and Eu speciation into carbides and their subsequent accumulation in the carbon-rich KP. Further work is necessary to extrapolate quantitative μO_2 values from quantitative EPMA data.
- The KP is approximately twice as thick in the safety-tested particle as compared to the as-irradiated particle. Additionally, the O:C ratio in the KP is higher in the safety-tested particle than in the as-irradiated particle. For both particles, the O:C is lower (< 0.5) in the thicker KP section on the non-gap side compared to the side with the gap. Thus, Sr, Ba, and Eu (as presumed carbides) appear in higher abundance in the non-gap side of both particles.
- It will be beneficial to re-evaluate this method using additional radial line scan data and mass balance calculations to better evaluate sample heterogeneity along the central plane. In addition, quantitative mid-plane X-ray mapping with extrapolation to the third dimension may yield more satisfactory results.
- Finally, this method could benefit by additional measurements performed on other particles in the same compact and other compacts to better assess its accuracy, add confidence to apparent trends in fission product distributions and behaviors, and identify areas for further improvement.

Declaration of Competing Interest

The authors declare that they have no known competing financial interests or personal relationships that could have appeared to influence the work reported in this paper.

CRediT authorship contribution statement

Karen E. Wright: Conceptualization, Project administration, Data curation, Formal analysis, Writing – original draft. **John Stempien:** Writing – original draft, Writing – review & editing. **Wen Jiang:** Visualization. **Isabella J. van Rooyen:** Funding acquisition, Writing – review & editing.

Acknowledgment

We thank Dr. Mitchell Meyer, of Idaho National Laboratory for his careful review and helpful suggestions and the National Scientific Users Facility for partial financial support. We also appreciate and acknowledge two anonymous reviewers whose thoughtful and insightful comments greatly improved this manuscript. This work was sponsored by the U.S. Department of Energy, Office of Nuclear Energy, under U.S. Department of Energy Idaho Operations Office Contract DE-AC07–05ID14517. The United States Government retains and the publisher, by accepting the article for publication, acknowledges that the United States Government retains a nonexclusive, paid-up, irrevocable, world-wide license to publish or reproduce the published form of this manuscript, or allow others to do so, for United States Government purposes.

Data availability

Data will be made available upon request.

Appendix A

Electron probe microanalysis was performed at Idaho National Laboratory's Irradiated Materials Characterization Facility using a Cameca SX100R electron probe microanalyzer, which is specifically designed for the analysis of highly radioactive specimens. To that end, the instrument's electronics and detectors are shielded to 3 Ci of ^{137}Cs.

Various peak and background counting times were employed depending on the phase type and element concentration. In all cases, the accelerating voltage was 20 kV and the beam was used in spot mode. The current employed for each element was 200 nA, except for Si in the SiC layer, which was measured using a current of 20 nA to avoid excessive detector dead time.

The choice of X-ray lines, standards, diffracting crystals, and corrected interferences is shown in Table A1. For some elements, an acceptable standard was not available. In this situation, a "virtual" standard was employed. The intensity for a virtual standard is determined by measuring the intensities of the same X-ray lines on the same crystal and spectrometer for elements that are adjacent on the periodic table to the X-ray line of interest. An X-ray intensity can then be computed for the line of interest.

Each X-ray line was measured using a peak and two backgrounds. The count time for each X-ray peak varied with the abundance and fluorescence yield of the element, but in general, each peak was counted for 300–500 s, with a background count

Table A1
The X-ray line, standard, diffracting crystal, and corrected interferences used for each measured element. Where no element is listed as an interference, no correction was made.

Element	X-ray line	Standard	Diffracting Crystal	Interferences Corrected
U	Mα	U	QTZ	Pd, Ru, Cd
Zr	Lα	Zr	PET	
La	Lα	LaP_5O_{14}	LiF	Cs, Nd
Ce	Lα	CeP_5O_{14}	LiF	Ba, Te
Nd	Lα	NdP_5O_{14}	LiF	Ce
Pr	Lα	PrP_5O_{14}	LiF	La, Sm
Sm	Lα	SmP_5O_{14}	LiF	Ce
Eu	Lα	EuP_5O_{14}	LiF	Pr, Nd
Ba	Lα	Barite	QTZ	Pr
Cs	Lα	Pollucite	PET	U, Ce, Te
Xe	Lα	Virtual	PET	Te, La
Mo	Lα	Mo	PET	
Ru	Lα	Ru	PET	Mo
Ag	Lβ	Ag_2Te	QTZ	Cd, U
Pd	Lα	Pd	QTZ	Ru, Mo, U
Te	Lα	Ag_2Te	PET	Cs, I
I	Lα	TlBrI	PET	Cd, Ba
Cd	Lα	Cd	QTZ	U, Ag
C	Kα	SiC	PC1	U
O	Kα	ThO_2	PC1	
Si	Kα	SiC	TAP	
Sr	Lα	$SrTiO_3$	TAP	Si

time approximately one-third of the peak time. For elements with higher count rates such as U in the kernel and Si in the SiC layer, the count rate was 20–30 s for the peak and 10–15 s for each background. Note that standards were not counted in the same manner as the sample points; the concentration of the element in the standard is generally so much higher than in the sample that it is not necessary to count for more than 30 s for the peak and 10 s for the background. Measuring the standards for the shorter time does not negatively impact quantification. In fact, if standards were measured at the same beam currents and for the same time period as the unknown sample, there would likely be excessive detector counter deadtime, which itself would negatively impact quantification. Finally, some standards, such as rare earth phosphates, are beam sensitive and are measured using a defocused 20 μm beam. All standards were measured using a 20 nA current, and the dead time for all analyses was set to 3 μS.

References

[1] Barnes, C., "AGR-2 fuel specification", Idaho National Laboratory Report, INL-SPC-923, rev. 3, January 9, (2009)

[2] J.D. Hunn, Data compilation for AGR-2 B&W UCO coated particle batch G73J-14-93073A". Oak Ridge National Laboratory Report, ORNL/TM-2008/134, Rev 1 (2008).

[3] J.D. Hunn, F.C. Montgomery, P.J. Pappano, Data compilation for AGR-2 B&W UCO compact lot LEU09-OP-Z". Oak Ridge National Laboratory Report, ORNL/TM-2010/017, Rev 1 (2010).

[4] J.D. Hunn, T.W. Savage, G.W.C. Silva, AGR-2 fuel compact pre-irradiation characterization summary report". Oak Ridge National Laboratory Report, ORNL/TM-2010/226, Rev 1 (2010).

[5] BWXT, "Industrial fuel fabrication and development lot G73I-14-69307". BWXT Data certification package, July 30, 2008.

[6] BWXT, "Industrial fuel fabrication and development lot G73J-14-93071A, G73J-14-93073A, G73J-14-93074A". BWXT Data certification package, September 12, 2008.

[7] BWXT, "Industrial fuel fabrication and development lot G73H-10-93085B". BWXT Data certification package, March 13, 2009.

[8] B. Collin, AGR-2 irradiation test final as-run report", Idaho National Laboratory Report, INL/EXT-14-32277, Rev 3 (2018).

[9] G. Helmreich, J. Hunn, J. McMurray, D. Brown, Enhanced method for analysis of individual UCO kernel phase fractions, Nucl. Eng. Des. (363) (2020) 110625.

[10] N. Ritchie, D. Newbury, J. Davis, EDS measurements of X-ray intensity at WDS precision and accuracy using a silicon drift detector, Micros. Microanal. 18 (2012) 892–904.

[11] M. Perrot, Microanalyse D'echantillons Irradies par La Microsonde de Castaing Application Au Combustible Nucleaire MOX, These Pour Obtenir Le Diplome, Universitaire Supèrieur de Recherche, Universite Paris Sud UFR Scientifique d'Orsay, 1995.

[12] H. Kleykamp, Mikrosondenuntersuchungen zum verhalten der spalprodukte in hoch abgebrannten htr-brennstoffen, Kernforschungszentrum Karlsruhe, Report KfK 2213 (1975).

[13] T. Tiegs, Fission product Pd-SiC interaction in irradiated coated particle fuels, Oak Ridge National Laboratory, ORNL/TM-7203, 1980.

[14] K. Minato, T. Ogawa, K. Fukuda, M. Shimizu, Y. Tayama, I. Takahashi, Fission product behavior in Triso-coated UO_2 fuel particles, J. Nucl. Mater. (208) (1994) 266–281.

[15] M. Barrachin, R. Dubourg, M. Kissane, V. Ozrin, Progress in understanding fission-product behaviour in coated uranium-dioxide fuel particles, J. Nucl. Mater. 385 (2009) 372–386 2009, doi:10.1016/j.nucmat.2008.12.025.

[16] M. Barrachin, R. Dubourg, S. DeGroot, M. Kissane, K. Bakker, Fission-product behaviour in irradiated TRISO-coated particles: results of the HFR-EUbis experiment and their interpretation, J. Nucl. Mater. (415) (2011) 104–116.

[17] K. Wright, I. Van Rooyen, Electron probe microanalysis of irradiated and 1600°C safety-tested agr-1 fuel particles with low and high retained ^{110m}Ag, in: Proceedings of the International Topical Meeting on High Temperature Reactor Technology (HTR 2016), Las Vegas, NV, 2016.

[18] Collin B., "AGR-2 irradiation experiment test plan", Idaho National Laboratory Report, INL/MIS-11-21682 (2018).

[19] R. Morris, J. Hunn, C. Baldwin, F. Montgomery, T. Gerczak, P. Demkowicz, Initial results from safety testing of US AGR-2 irradiation test fuel, Nucl. Eng. Des. (329) (2018) 124–133.

[20] Hunn, J.D., Gerczak, T.J., Morris, R.N., Baldwin, C.A., Montgomery, F.C., "PIE on safety-tested loose particles from compact 4-4-2". Oak Ridge National Laboratory Report, ORNL/TM-2015/161 (2016).

[21] C.A. Baldwin, J.D. Hunn, R.N. Morris, F.C. Montgomery, C.M. Silva, P.A. Demkowicz, First elevated-temperature performance testing of coated particle fuel compacts from the AGR-1 irradiation experiment, Nucl. Eng. Des. 271 (2014) 131–141.

[22] T.J. Gerczak, J.D. Hunn, R.N. Morris, F.C. Montgomery, D.J. Skitt, C.A. Baldwin, J.A. Dyer, B.D. Eckhart, Analysis of fission product distribution and composition in the TRISO layers of AGR 2 fuel, Nucl. Eng. Des. 364 (2020) 110656.

[23] P. Demkowicz, J. Hunn, R. Morris, I. van Rooyen, T. Gerczak, J. Harp, S. Ploger, AGR-1 post irradiation examination final, report INL/EXT-15-36407, (2015).

[24] Hawkes G., "AGR-2 daily as-run thermal analyses", ECAR-2476, Idaho National Laboratory Report, INL/MIS-14-31871, (2014).

[25] I. van Rooyen, Y. Yang, Z. Fu, B. Kombaiah, K. Wright, Advanced Microscopy Report on UCO Fuel Kernels from Selected AGR-1 and AGR-2 Experiments, Idaho National Laboratory External, 2021 Report INL/EXT-21-00947.

[26] J. Sterbentz, JMOCUP As-Run Daily Depletion Calculation for the AGR-2 Experiment in the ATR B-12 Position, Idaho National Laboratory, 2014 ECAR-2066.

[27] Hawkes G., "AGR-2 irradiation experiment thermal projections", Idaho National Laboratory Report, ECAR-1692, (2012)

[28] J. Pouchou, F. Pichoir, K.F.J. Heinrich, D.E. Newbury, Quantitative analysis of homogeneous or stratified microvolumes applying the model," "PAP", in: Electron Probe Quantification, Plenum Press, New York, 1991, pp. 31–76.

[29] I. Farthing, C. Walker, Heinrich's Mass Absorption Coefficients for the K, L, and M Lines, The European Commission, Institute for Transuranium Elements, Karlsruhe, 1990 Report K0290140.

[30] P. Poeml, X. Llovet, Determination of mass attenuation coefficients of Th, U, Np, and Pu for Oxygen Kα X-rays using and electron microprobe, Micros. Microanal. 26 (2020) 194–203.

[31] Collin, B. "AGR-2 irradiation experiment test plan", Idaho National Laboratory, PLN-3798, rev. 2, INL/MIS-11-21682 (2018).

[32] J. Bower, S. Ploger, P. Demkowicz, J. Hunn, Measurement of kernel swelling and buffer densification in irradiated UCO-TRISO particles, J. Nucl. Mater. (486) (2017) 339–349.

[33] Casino v. 2.51, 2017, Copyright Universite De Sherbrooke, Sherbrooke, Quebec, Canada

[34] J. Hunn, C. Baldwin, T. Gerczak, F. Montgomery, R. Morris, C. Silva, P. Demkowicz, J. Harp, S. Ploger, Detection and analysis of particles with failed SiC in AGR-1 fuel compacts, Nucl. Eng. Des. 306 (306) (2016) 36–46.

[35] W. Schenk, H. Nabielek, High-temperature fission product release and distribution at 1600 to 1800 °C, Nucl. Technol. (96) (1991) 323–336.

[36] I. van Rooyen, D. Janney, B. Miller, P. Demkowicz, J Riesterer, Electron microscopic evaluation and fission product identification of irradiated TRISO coated particles from the AGR-1 experiment: a preliminary review, Nucl. Eng. Des. 271 (2014) 114–122.

[37] F. Homan, T. Lindemer, E. Long Jr, T. Tiegs, R. Beatty, Stoichiometric effects on performance of high-temperature gas-cooled reactor fuels from the U-C-O System, Nucl. Tech. (35) (1977) 428–441.

[38] R. Seibert, K. Terrani, D. Velazquez, J. Hunn, C. Baldwin, F. Montgomery, J Terry, Local atomic structure of Pd and Ag in the SiC Containment layer of TRISO fuel particles fissioned to 20% burn-up, J. Nucl. Mater. (500) (2018) 316–326.

[39] T. Lillo, I. van Rooyen, Associations of Pd, U and Ag in the SiC layer of neutron-irradiated TRISO fuel, J. Nucl. Mater. 460 (460) (2015) 97–106.

[40] F. Rice, J. Stempien, P. Demkowicz, Ceramography of irradiated TRISO fuel from the AGR-2 experiment, Nucl. Eng. Des. 329 (329) (2018) 73–81.

[41] Stempien J., Plummer M., and Schulthess J., "Measurement of kernel swelling and buffer densification in irradiated UCO and UO2 TRISO fuel particles from AGR-2", Idaho National Laboratory Report, INL/EXT-19-54502, June 2019.

[42] S. Ploger, P. Demkowicz, J. Hunn, J. Kehn, Microscopic analysis of irradiated AGR-1 coated fuel compacts, Nucl. Eng. Des. 271 (271) (2014) 221–230.

[43] S. Meher, I. van Rooyen, C Jiang, Understanding of fission products transport in the SiC layer of TRISO fuels by nanoscale characterization and modeling, J. Nucl. Mater. 527 (2019) 151793.

[44] H. Grubmeier, A. Naoumidis, B. Thiele, Silicon carbide corrosion in high-temperature gas-cooled reactor fuel particles, Nucl. Technol. 35 (2) (1977) 413–427.

[45] High Temperature Gas Cooled Reactor Fuels and MaterialsInternational Atomic Energy Commission Report, IAEA-TECDOC, Vienna, 2010 1645.

[46] G. Miller, D. Petti, J. Maki, D. Knudson, W. Skerjanc, PARFUME Theory and Model Basis Report, Idaho National Laboratory External, 2018 Report, INL/EXT-08-14497.

[47] R. Williamson, J. Hales, S. Novascone, G. Pastore, K. Gamble, B. Spencer, W. Jiang, S. Pitts, A. Casagranda, D. Schwen, A. Zabriskie, A. Toptan, R. Gardner, C. Matthews, W. Liu, H. Chen, BISON: a flexible code for advanced simulation of the performance of multiple nuclear fuel forms, Nucl. Technol. (2021), doi:10.1080/00295450.2020.1836940.

[48] J. Hales, R. Williamson, S. Novascone, D. Perez, B. Spencer, G. Pastore, Multidimensional multiphysics simulation of TRISO particle fuel, J. Nucl. Mater. 443 (1) (2013) 531–543.

[49] W. Jiang, J. Hales, B. Spencer, B. Collin, A. Slaughter, S. Novascone, A. Toptan, K. Gamble, R. Gardner, TRISO particle fuel performance and failure analysis with BISON, J. Nucl. Mater. 548 (2021) 152795.